Nano Trends 8 (2024) 100062

Contents lists available at ScienceDirect

Nano Trends

journal homepage: www.elsevier.com/locate/nantre

Nanogenerators via dynamic regulation of electrical double layer

Xiang Li [a,b], Zhong Lin Wang [a,c,d,*], Di Wei [a,e,*]

[a] Beijing Institute of Nanoenergy and Nanosystems, Chinese Academy of Sciences, Beijing 101400, PR China
[b] School of Nanoscience and Engineering, University of Chinese Academy of Sciences, Beijing 100049, PR China
[c] Beijing Key Laboratory of Micro-Nano Energy and Sensor, Center for High-Entropy Energy and Systems, Beijing Institute of Nanoenergy and Nanosystems, Chinese Academy of Sciences, Beijing 101400, PR China
[d] Guangzhou Institute of Blue Energy, Knowledge City, Huangpu District, Guangzhou 510555, PR China
[e] Centre for Photonic Devices and Sensors, University of Cambridge, 9 JJ Thomson Avenue, Cambridge CB3 0FA, UK

ARTICLE INFO

Keywords:
Water-based energy harvesting
Electrical double layer
Dynamic regulation
Stern layer
Diffuse layer

ABSTRACT

The world is grappling with dual crises of energy depletion and environmental degradation, as escalating global energy demands strain the sustainability of existing systems. While traditional energy harvesting technologies such as wind, solar, and hydropower have progressed, challenges in energy storage and system stability persist, underscoring the urgent need for more efficient and sustainable alternatives. Emerging water-based energy harvesting technologies that harness the dynamic regulation of electrical double layers (EDLs) at solid-liquid interfaces offer significant advantages, including enhanced energy conversion efficiency and flexible application potential. These systems are particularly well-suited to meet the growing demand for distributed energy in the Internet of Things (IoT), where adaptable and scalable energy solutions are essential. Key nanogenerator technologies utilizing dynamic EDL regulation are classified into five major types: solid-liquid triboelectric nanogenerators (S-L TENGs), triboiontronic nanogenerators (TINGs), hydrovoltaic technology, moisture-enabled electric generators (MEGs), and osmotic power sources. This review provides a comprehensive analysis of their operating principles, output characteristics, and typical applications. Furthermore, it addresses the main challenges and bottlenecks these technologies face and outlines future research and development opportunities, advancing the field of water-based energy harvesting.

1. Introduction

Amid the intensifying global energy crisis and worsening environmental pollution, the excessive dependence on fossil fuels not only accelerates resource depletion [1–4], but also aggravates climate change and environmental degradation [5–7], resulting in global warming [8–10], extreme weather events [11–13], and ecological imbalances [14–16]. Meanwhile, the ever-increasing energy demand puts immense pressure on the existing energy supply systems [17–19], highlighting the urgent need for alternative renewable energy solutions [20–24]. While solar energy [25–27] and wind energy [28–31], as leading renewable energy sources, provide substantial environmental benefits and resource renewability [32–35], they are not without limitations. Solar energy is highly dependent on sunlight conditions [36–38], while wind energy is constrained by factors such as wind speed variability and terrain [39–41], all of which can limit efficiency and consistent power output, leading to unstable power generation in certain regions. Moreover, the infrastructure for these energy sources may also have environmental impacts, such as land use [42–44] and ecological disturbance [45–47]. In contrast, water-based energy, as a rich and diverse natural resource [48–51], presents notable advantages. It can provide a stable power supply from various sources, including the river [52–54], lake [55–57], ocean [58–61], tide [62–64], humidity [65–69], rain [70–72], and evaporation [73–76], under different environmental conditions. However, traditional hydropower technologies face challenges such as geographical limitations [77], ecological impacts [78], and high costs [79], which restrict their widespread application. Therefore, there is a pressing need to develop new types of water-based power generation technologies. These innovative technologies have the potential to overcome the limitations of traditional hydropower, offering more flexible, environmentally friendly, and efficient energy solutions. Advancing these technologies will enable more effective harnessing and utilization of water-based energy resources, offering viable solutions to mitigate the energy crisis and environmental pollution, and steering the

* Corresponding authors at: Beijing Institute of Nanoenergy and Nanosystems, Chinese Academy of Sciences, Beijing 101400, PR China.
E-mail addresses: zhong.wang@mse.gatech.edu (Z.L. Wang), dw344@cam.ac.uk (D. Wei).

https://doi.org/10.1016/j.nwnano.2024.100062
Received 24 October 2024; Received in revised form 24 November 2024; Accepted 24 November 2024
Available online 26 November 2024

global energy system toward a more sustainable future.

In natural environments, the abundance of water-based energy resources is evident not only in the widespread distribution of water bodies but also in the diverse solid-liquid interfaces [80–82]. The dynamic regulation of these interfaces provides innovative avenues for the development of new water-based power generation technologies [72,83,84]. In particular, the electrical double layer (EDL) [85–89], as a fundamental mechanism at solid-liquid interfaces, plays a crucial role in influencing charge distribution and potential regulation [90–94]. By dynamically regulating the EDL, energy conversion efficiency can be optimized, unlocking new avenues for fully harnessing and utilizing water-based energy resources [95–97]. The development of EDL theory has progressed through several key stages. Helmholtz initially proposed the concept of the EDL, describing the charge distribution at electrode surfaces [85]. Subsequently, Gouy and Chapman introduced the concept of the diffuse layer, considering ion distribution and potential decay in electrolyte solutions [86,87]. Stern further refined this with considerations of ion size, leading to the more comprehensive Gouy-Chapman-Stern model [88,89]. These theories have laid the theoretical foundation for new water-based power generation technologies based on the dynamic regulation of EDL. On the other hand, traditional EDL models primarily focus on conductor-liquid interfaces. Recent advancements in the "two-step" model have expanded EDL theory to dielectric-liquid interfaces [98–100], thereby enriching the theoretical foundation and offering new possibilities for material selection in innovative water-based power generation technologies. This extension facilitates enhanced utilization of the EDL properties of various materials, significantly improving the efficiency and adaptability of water-based energy technologies [101–104]. In light of the increasing demand for efficient distributed energy nodes within smart devices and the Internet of Things (IoT) systems [105–107], nanogenerator technologies that leverage the dynamic regulation of EDL for effective water-based energy harvesting have been extensively developed. These technologies provide remarkable flexibility and high efficiency, making them highly pertinent to contemporary energy applications. Consequently, a comprehensive review of the types, principles, characteristics, and applications of these nanogenerator technologies is imperative.

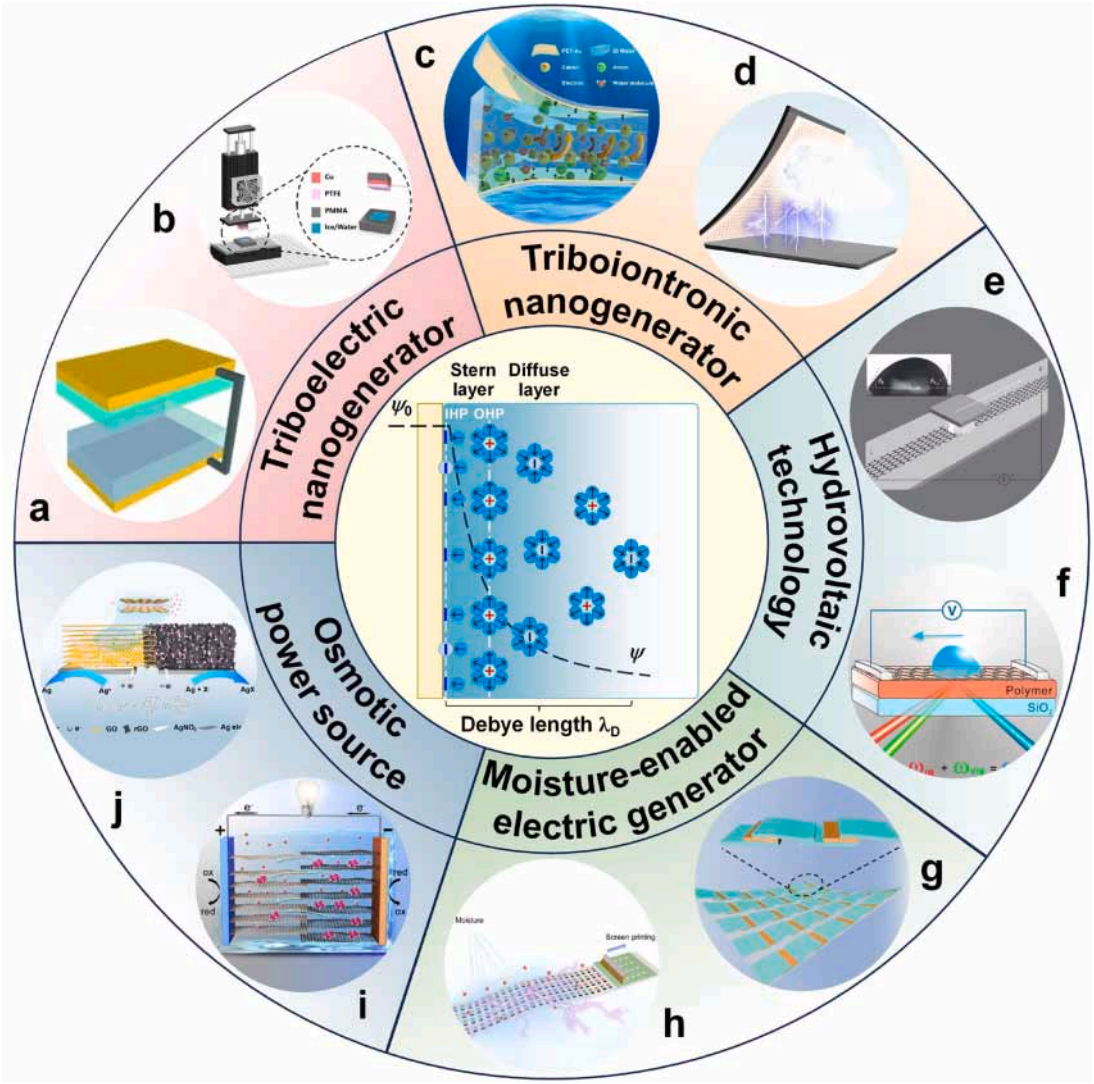

Fig. 1. The nanogenerator technologies via dynamic regulation of EDL were classified into five major types. a, b, S-L TENGs [142,143]. c, d, TINGs [95,96]. e-f, Hydrovoltaic technology [144,145]. g, h, MEGs [74,146]. i, j, Osmotic power sources [147,148]. a, Copyright 2013, WILEY-VCH. b, Copyright 2024, Elsevier Ltd. c, Copyright 2024, The Author(s). Distributed under the terms of the Creative Commons CC BY license. d, Copyright 2023, Elsevier Inc. e, Copyright 2014, Springer Nature Limited. f, Copyright 2018, American Chemical Society. g, Copyright 2021, The Author(s), Distributed under exclusive licence to Springer Nature Limited. h, Copyright 2023, Elsevier Inc. i, Copyright, 2021, The author(s) retains copyright to individual articles, and the NAS retains an exclusive license to publish these articles and holds copyright to the collective work. j, Copyright 2024, Elsevier Inc.

In this review, the key nanogenerator technologies via dynamic regulation of EDL were comprehensively summarized, which were classified into five major types (Fig. 1): solid-liquid triboelectric nanogenerators (S-L TENGs), triboiontronic nanogenerators (TINGs), hydrovoltaic technology, moisture-enabled electric generators (MEGs), and osmotic power systems. Firstly, S-L TENGs operate by manipulating the charge distribution on the EDL near dielectric materials through mechanical motion or electrostatic fields. This category can be further subdivided into mechanically driven direct current (DC) S-L TENGs [83, 108], mechanically driven alternating current (AC) S-L TENGs [109–112], and electrostatically driven AC S-L TENGs [113–115]. These devices exploit the high internal resistance of dielectric materials to generate high-voltage outputs. Secondly, TINGs could achieve effective pulsed DC outputs by either creating asymmetric EDLs at the ultra-thin conductor-liquid interface on dielectric substrates [96] or by regulating the charge density in the diffuse layer of the EDL adjacent to the dielectric surface [95]. Thirdly, hydrovoltaic technology generates a constant current by mechanically manipulating the boundary of the EDL at the ultra-thin conductor-liquid interface on dielectric substrates [116–118], enabling continuous power output, which is particularly suitable for sustained energy applications. Fourthly, MEGs could drive the directional migration of ions within the Debye length range of the EDL through humidity-induced functional group hydrolysis creating an ion concentration gradient [119–122], or by facilitating the evaporation-driven transport of specific polar ions through charged ion channels [123–125]. This mechanism allowed for the independent generation of constant current output in a more convenient manner. Fifthly, conventional osmotic power sources utilize concentration gradients between solutions to drive the movement of specific-polarity ions within the Debye length of the EDL at ion channel surfaces [126–128], resulting in large-scale stable power outputs. In particular, two-dimensional (2D) nanofluidic channels exhibit enhanced ionic mobility and permeability due to the anomalous ion dynamics in nanoconfined environments [129–131], significantly boosting the power output of osmotic power sources. Furthermore, the practical application scenarios of these nanogenerator technologies were analyzed in various fields of water-based energy harvesting [132–141]. This review aims to provide insights into the selection of appropriate nanogenerator technologies for different use cases, optimizing their performance in real-world applications.

2. Advancements in EDL model evolution

In emerging water-based energy harvesting technologies, the dynamic regulation of the EDL is regarded as a pivotal strategy for enhancing energy collection efficiency, thereby establishing a theoretical foundation for the advancement of more efficient water-based technologies. The evolution of EDL theory has experienced a continuous process of refinement. The earliest EDL model was proposed by Helmholtz in the 19th century [85], which analogized the charge

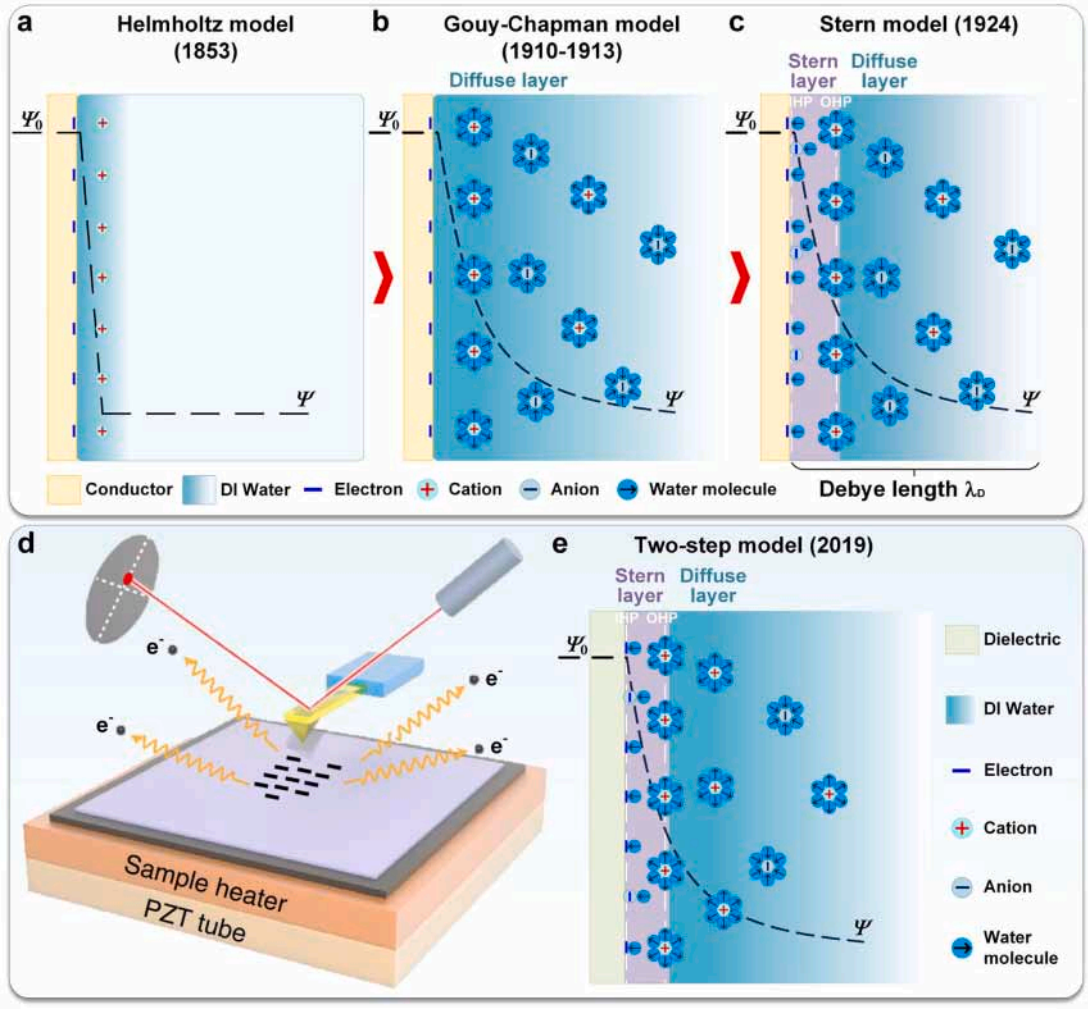

Fig. 2. The evolution of the EDL model. a–c, The Helmholtz model, the Gouy-Chapman model, and the Stern model [92]. d, The electron and ion transfer at the liquid-dielectric interface was systematically investigated by Lin et al. in 2020 [99]. e, The "two-step" EDL model [92]. a–c, and e, Copyright 2024, WILEY-VCH. d, Copyright 2020, The Author(s). Distributed under the terms of the Creative Commons CC BY license.

distribution at the solid-liquid interface to that of a parallel-plate capacitor (Fig. 2a). According to this model, ions in the liquid form a tightly packed layer of charge near the solid surface, balanced by an equivalent charge on the solid. While this model established a foundational framework for understanding interfacial electrical phenomena, it did not incorporate the thermal motion and diffusion of ions in solution, thereby neglecting the dynamic behavior of the EDL. In the early 20th century, Gouy and Chapman independently expanded on the Helmholtz EDL model by introducing the concept of a diffuse layer [86,87] (Fig. 2b). They proposed that ions not only form a dense layer near the solid surface but also diffuse away from the interface according to probabilistic distributions. The Gouy-Chapman model introduced the idea of charge density decaying exponentially with distance, thereby capturing the dynamic nature of the EDL and offering a more realistic description of ion behavior in solution. However, the model had its own limitations, particularly in neglecting the size of ions and their specific adsorption onto the surface. To rectify these limitations, the Gouy-Chapman-Stern model, commonly referred to as the Stern model, was introduced in 1924 [88,89] (Fig. 2c), which combined aspects of both the Helmholtz and Gouy-Chapman models. It divided the EDL into two distinct regions: a compact Stern layer, where ions are either adsorbed onto the solid surface or solvated close to it, and a diffuse layer, where ions follow the distribution described by the Gouy-Chapman model. This hybrid approach retained the static capacitance concept of Helmholtz while incorporating the dynamic ion diffusion behavior from the Gouy-Chapman model, offering a more comprehensive and accurate depiction of the EDL. These theoretical advancements have deepened our understanding of the dynamic regulation of the EDL at solid-liquid interfaces, providing critical insights for modern electrochemical systems and water-based energy harvesting technologies. The ability to manipulate the EDL has proven essential for optimizing charge transfer and enhancing energy conversion efficiency, paving the way for innovative nanogenerator designs based on EDL dynamics.

The aforementioned traditional EDL models primarily emphasized ion transfer at conductor-liquid interfaces. However, the charge transfer mechanisms at liquid-dielectric interfaces are significantly more complex than those characterized by these models. Recent research conducted by Lin et al. employed silicon dioxide (SiO_2) as the solid material to systematically examine electron and ion transfer at the liquid-dielectric interface [99,149,150] (Fig. 2d). Their experiments demonstrated that contact electrification (CE) between the liquid and the SiO_2 surface induces both electron and ion transfer, with notable variations observed at different temperatures. Specifically, as the temperature increased, electrons were thermally excited and emitted from the SiO_2 surface, while ions remained bound to the SiO_2 surface due to strong covalent bonding. The study indicated that electron transfer predominates on the SiO_2-liquid interface, accounting for 77% of the total charge, while ion transfer constitutes 23%. Additionally, the hydrophilicity of the solid surface significantly affected the ratio of charge transfer. Higher hydrophilicity materials interacted more strongly with ions in the liquid, leading to a higher proportion of ion transfer, whereas lower hydrophilicity materials tended to involve more electron transfer due to weaker interactions with the liquid. These findings highlighted the complex nature of charge transfer at liquid-dielectric interfaces and led to the proposal of a new "two-step" EDL model at the dielectric-liquid interface [98–100] (Fig. 2e). In the first step, when the liquid contacted a pristine solid surface, molecules and ions (such as H_2O, cations, and anions) impacted the solid surface due to thermal motion and liquid pressure. During this impact, electron transfer occurred between the solid atoms and water molecules due to overlapping electron clouds, and ionization reactions might also take place, generating both electrons and ions that are simultaneously adsorbed on the solid surface and forming the inner Helmholtz plane (IHP). In the second step, the majority of opposite ions in the liquid were attracted to and migrated toward the charged surface by electrostatic interactions, forming the outer Helmholtz plane (OHP). Together, these layers constituted the Stern layer, while a few opposite ions nearby formed the diffuse layer, resulting in a complete EDL. This model offered a new perspective on liquid-solid charge transfer and provided valuable theoretical and practical guidance for the development of novel water-based energy harvesting technologies and related applications.

3. Various types of S-L TINGs

In the field of S-L TENGs, these devices functioned by modulating the charge distribution within the EDL formed at the interface between a liquid and a dielectric material. This modulation was achieved through mechanical motion or the application of electrostatic fields. S-L TENGs could be broadly classified into three categories: mechanically driven DC S-L TENGs, mechanically driven AC S-L TENGs, and electrostatically driven AC S-L TENGs. Each category exhibited distinct output characteristics and application potential. In particular, S-L TENGs could leverage the high internal resistance of dielectric materials to achieve high-voltage outputs, making them promising candidates for energy scavenging and sustainable power generation. Their adaptability and efficiency in converting diverse forms of energy position them as vital components in future smart systems and IoT applications.

3.1. *Mechanically driven DC S-L TENGs*

Various types of S-L TENGs could be operated by manipulating the charge distribution in the EDL near dielectric materials through mechanical motion or electrostatic fields. In mechanically driven DC S-L TENGs, the process of power generation as the liquid moved across the dielectric surface was intricately linked to the CE effect and the dynamic behavior of the EDL. When the liquid first came into contact with the dielectric surface with higher electronegativity, charge transfer occurred at the solid-liquid interface, forming a negatively charged Stern layer that adheres closely to the dielectric material (Fig. 3a). Concurrently, cations in the diffuse layer remained distributed throughout the liquid, as described by the "two-step" EDL model. As the liquid continued to slide on the dielectric surface, mechanical forces drove the directional migration of these cations, causing the EDL boundary to advance along the surface. This migration of cations induced a continuous movement of charge carriers within the liquid. When the liquid subsequently moved away from the dielectric surface, the cations in the diffuse layer came into contact with the electrode (Fig. 3b). This interaction leads to a redistribution of charges, generating a unidirectional flow of electrons in the external circuit and thereby producing a stable DC output. The power generation remained continuous as long as the liquid was in motion, dynamically adjusting the charge distribution within the diffuse layer. This process not only initiated charge transfer but also sustained a consistent DC output until a stable EDL was formed. Such a mechanism provided a robust foundation for efficient energy harvesting and precise surface charge regulation, demonstrating the potential of S-L TENGs for practical applications in energy generation and sensor technologies.

In 2015, a microfluidic generator (MFG) was developed by Zhang et al. as a representative example of a DC S-L TENG [108] (Fig. 3c). The device utilized a microfluidic chip made from polydimethylsiloxane (PDMS), featuring a quasi-porous structure that allows a 1 μM potassium chloride (KCl) aqueous solution to flow through. Experimental studies focused on the impact of flow rate on the current output, revealing a nearly linear relationship between the current and flow rate (Fig. 3d). As the flow rate increased from 0 to 0.4 mL/min, the current output exhibited a positive correlation, while reversing the flow direction resulted in a corresponding negative change in current output. Additionally, when the KCl concentration was below 10 μM, the short-circuit current (I_{SC}) stabilized at approximately 2.45 nA, but it dramatically decreased at higher concentrations (Fig. 3e). This decrease is attributed to the formation of a dense EDL near the dielectric surface, resulting from elevated ion concentrations that screen and impede electron transfer between the solid and liquid, thereby significantly

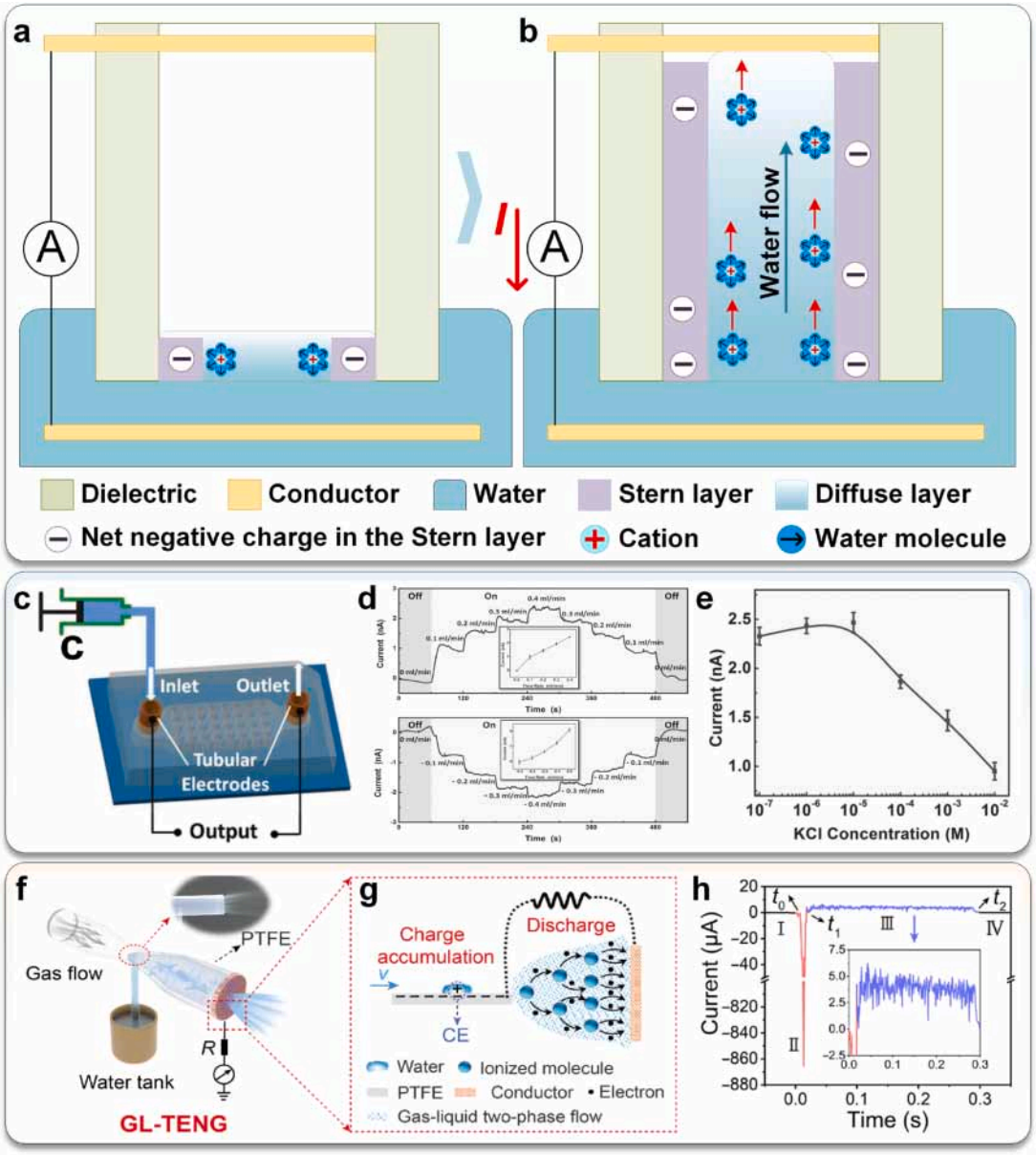

Fig. 3. The operating mechanism of mechanically driven DC S-L TENGs and the output characteristics of typical devices. a and b, The operating mechanism of mechanically driven DC S-L TENGs. c, In 2015, a microfluidic generator (MFG) was developed by Zhang et al. as a representative example of a DC S-L TENG [108]. d, There was an approximate linear relationship between the output current and flow rate. e, When the KCl concentration was below 10 μM, the I_{SC} stabilized at approximately 2.45 nA, but it dramatically decreased at higher concentrations. f, The GL-TENG was developed by Dong et al. in 2022 [151]. g, This device combined the CE and breakdown effect by utilizing the interaction between high-speed airflow and liquid to create a gas-liquid two-phase flow. h, The GL-TENG could achieve a peak I_{SC} of 867 μA. c–e, Copyright 2015, WILEY-VCH Verlag GmbH & Co. KGaA. f-h, Copyright 2022, American Association for the Advancement of Science. Distributed under a Creative Commons Attribution NonCommercial License.

compromising output performance. These results demonstrated the stability and reliability of the MFG in low-concentration solutions and its potential as an effective self-powered flow sensor. Based on the above experiment, the formation of a dense EDL close to the dielectric surface could significantly screen the solid-liquid interface, severely limiting the output performance of conventional DC S-L TENGs. To address this issue, the dielectric breakdown effect was introduced, which could disrupt the dense EDL once the charge accumulation reached a certain threshold, thereby restoring charge transfer. Based on this principle, the gas-liquid two-phase flow-based triboelectric nanogenerator (GL-TENG) was developed by Dong et al. in 2022 [151] (Fig. 3f). This device combined the CE and breakdown effect by utilizing the interaction between high-speed airflow and liquid to create a gas-liquid two-phase flow (Fig. 3g). When the accumulated charge on the polytetrafluoroethylene (PTFE) surface reached a sufficient level, the breakdown voltage of the gas-liquid two-phase flow was lower than that of air, allowing for effective disruption of the EDL and large-scale charge transfer. Experimental results indicated that the GL-TENG could achieve a peak I_{SC} of 867 μA and a peak open-circuit voltage (V_{OC}) of 3789 V in a single cycle (Fig. 3h), respectively. Furthermore, the GL-TENG could operate stably for over 10,000 cycles and power 1500 LEDs. Based on charge accumulation due to solid-liquid contact and effective breakdown currents, mechanically driven DC S-L TENGs could effectively overcome the performance limitations imposed by dense EDL, achieving higher current and voltage outputs and demonstrating significant application potential.

3.2. Mechanically driven AC S-L TENGs

In addition to alleviating the screening effect of dense EDLs on solid-liquid charge transfer through the incorporation of dielectric breakdown, mechanically driven AC S-L TENGs can generate AC output more flexibly by manipulating the movement of the Stern layer near the dielectric surface. This control over the Stern layer dynamically modulates the charge distribution in the diffuse layer within the liquid,

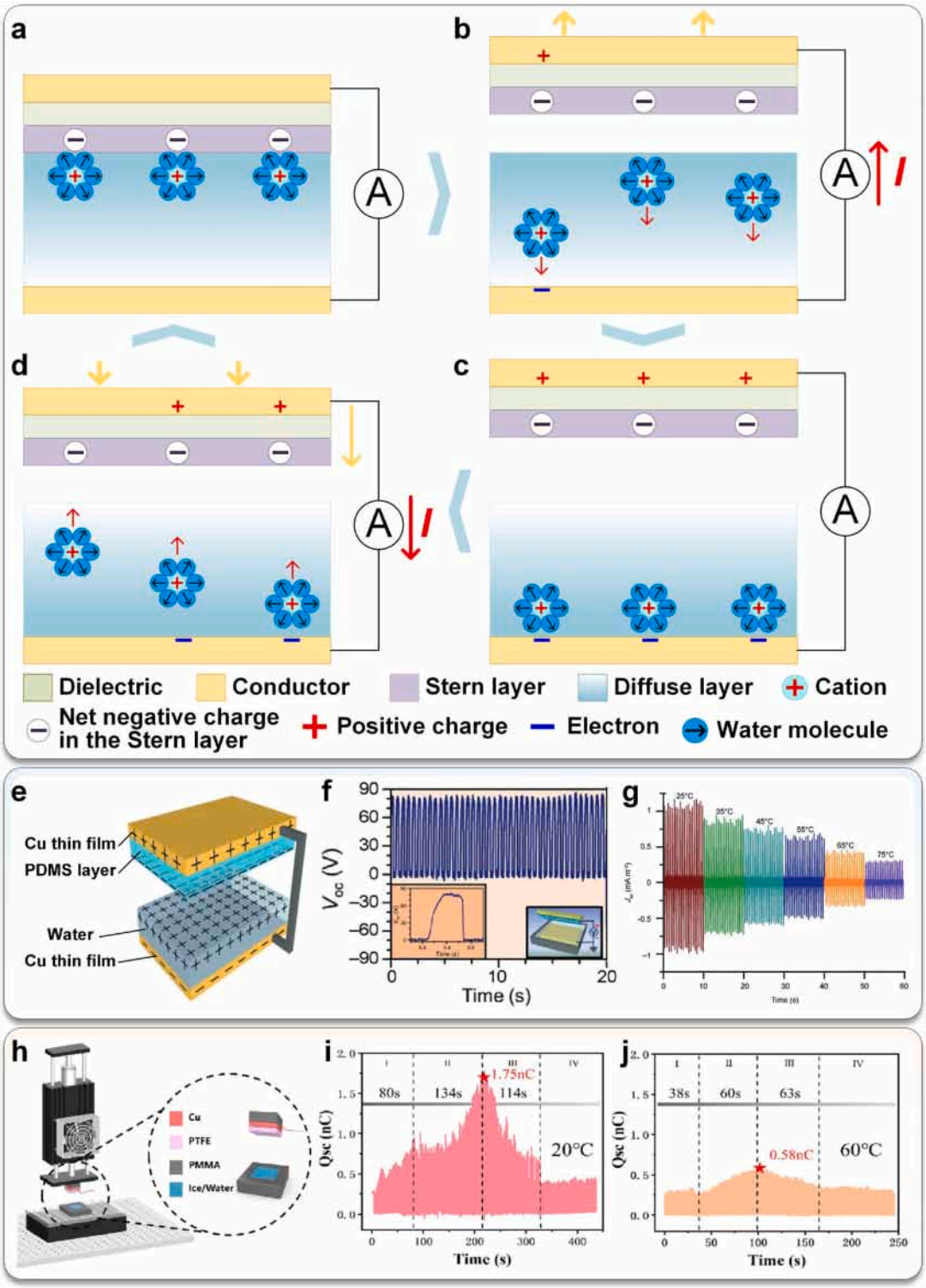

Fig. 4. The operating mechanism of mechanically driven AC S-L TENGs and the output characteristics of typical devices. a–d, The operating mechanism of mechanically driven AC S-L TENGs.e, In 2013, a typical mechanically driven AC S-L TENG via the PDMS pyramid array was developed by Lin et al. [142]. f, Its V_{OC} could be up to 52 V. g, The I_{SC} density decreased from 1.05 mA/m^2 at 25 °C to 0.28 mA/m^2 at 75 °C. h, Wei et al. conducted a study in 2024 to further explore the influence of temperature on the formation of the EDL [143]. i, The Q_{SC} initially increased and then decreased during the melting process. j, As the ambient temperature rose to 60 °C, the accelerated ion movement facilitated a faster formation of the EDL during the melting process. e-g, Copyright 2013, WILEY-VCH. h-j, Copyright 2024, Elsevier Ltd.

effectively harnessing the dynamic processes of charge accumulation and release at the solid-liquid interface. During the operation of AC S-L TENGs, when the liquid made contact with the dielectric surface with higher electronegativity, a stable EDL was formed (Fig. 4a). The Stern layer, characterized by a net negative charge, was tightly adsorbed onto the dielectric surface, while cations from the liquid were primarily concentrated in the diffuse layer near the Stern layer, creating a spatially distributed charge region. The interface charge between the solid and liquid was balanced. As mechanical motion drove the dielectric away from the liquid, the interaction between the Stern and diffuse layers weakened, and the cations became less tightly bound to the surface. The net negative charge in the Stern layer induced electron transfer in the external circuit via electrostatic induction, generating a forward current (Fig. 4b). Once the dielectric was fully separated from the liquid, the electron transfer was completed, and the system reached a new equilibrium state (Fig. 4c). When the dielectric re-approached the liquid, the cations migrated back toward the Stern layer, re-establishing the EDL (Fig. 4d). This process triggered a reverse flow of electrons in the external circuit, producing a reverse current. Through the continuous cycle of solid-liquid contact and separation, mechanically driven AC S-L TENGs exploited the interactions between the Stern and diffuse layers to produce AC output efficiently.

As early as 2013, a typical mechanically driven AC S-L TENG [142] (Fig. 4e) based on the polydimethylsiloxane (PDMS) pyramid array was developed by Lin et al. It could efficiently harness the dynamic interactions between the Stern and diffuse layer at the solid-liquid interface to generate alternating current. When the patterned PDMS pyramid array contacted water, an EDL was established. The mechanical motion facilitated a cyclic process of charge accumulation and release, generating an impressive V_{OC} of up to 52 V (Fig. 4f), an I_{SC} density of 2.45 mA/m^2, and a peak power (P_R) density of nearly 0.13 W/m^2, sufficient to power 60 commercial light-emitting diodes (LEDs) simultaneously. Additionally, the study highlighted the influence of temperature on the electrical output, with the I_{SC} density decreasing from 1.05 mA/m^2 at 25 °C to 0.28 mA/m^2 at 75 °C (Fig. 4g). This reduction might be attributed to enhanced ion mobility at elevated temperatures, leading to a denser EDL formation that acts as a screening layer, thereby reducing the interaction with charges in the diffuse layer and diminishing charge transfer efficiency. To further explore the influence of temperature on the formation of the EDL, Wei et al. conducted a study in 2024 examining the phase transition of ice melting into water at various ambient temperatures and its effect on the charge transfer between ice and PTFE dielectric material [143] (Fig. 4h). At a room temperature of 20 °C, the transferred charge (Q_{SC}) initially increased and then decreased during the melting process (Fig. 4i). In the initial melting stage, where solid-solid (S-S) contact predominated, the formation of micro-droplets on the ice surface enhanced the contact area with the PTFE, resulting in a continuous increase in electron transfer. This led to a peak Q_{SC} of approximately 1.75 nC at around 214 s. As the melting progressed to the partial melting stage, the formation of numerous droplets transitioned the contact to solid-liquid, where the gradually developing EDL began to screen the charge transfer, resulting in a decline in Q_{SC}. Once the ice completely melted into the water, a stable but diminished output was observed due to the dynamic nature of the EDL. Moreover, as the ambient temperature rose to 60 °C (Fig. 4j), the accelerated ion movement facilitated a faster formation of the EDL during the melting process. This resulted in the peak Q_{SC} being reached more quickly, at 98 s, but the peak value decreased to only 0.58 nC due to the enhanced screening effect. These experiments not only elucidated the dynamic mechanisms of charge transfer during the melting of ice but also provided critical insights into the influence of temperature on the formation of the EDL, thereby offering a theoretical basis for optimizing energy harvesting and self-powered sensor technologies via mechanically driven AC S-L TENGs.

3.3. Electrostatically driven AC S-L TENGs

Conventional S-L TENGs experienced performance instability due to liquid evaporation, which altered the dielectric properties and compromised the stability of the EDL, ultimately diminishing charge transfer efficiency and output performance. To address this issue, a sealed design could be employed to minimize evaporation, while encapsulating the liquid with highly electronegative dielectric materials ensures its stability and promotes the formation of a dense EDL. By dynamically modulating the charge distribution within the EDL using an external electrostatic field, the electrostatically driven AC S-L TENG could be developed, significantly enhancing both output performance and system stability. The working principle of electrostatically driven AC S-L TENGs could be divided into four stages. Firstly, the liquid came into contact with dielectric I, forming an EDL (Fig. 5a). Simultaneously, the backside of dielectric I contacted the more electronegative dielectric II, resulting in the transfer of electrons from dielectric I to the surface of dielectric II, leaving dielectric I positively charged. Secondly, when dielectric I and II separated (Fig. 5b), the positive charge on the surface of dielectric I generated an electric field that drove cations in the diffuse layer away from the dielectric I-liquid interface. These cations ultimately adsorbed onto the conductor electrode surface, facilitating the transfer of electrons from the ground to the electrode, thus generating a positive current. Thirdly, once dielectric I and II were completely separated (Fig. 5c), the electric field reached equilibrium, and electron transfer ceased. Finally, when dielectric II approached dielectric I again (Fig. 5d), the electric field on the surface of dielectric I was gradually balanced, allowing cations to return, which generated a reverse current in the external circuit. With continuous mechanical stimulation, electrostatically driven AC S-L TENGs could reliably produce alternating current. The sealed design effectively minimized liquid evaporation, thereby ensuring dielectric stability and reliability, which enhance s energy conversion efficiency. Furthermore, this design enables the generator to adapt to diverse environmental conditions, facilitating efficient energy conversion across various applications.

The shape-adaptive TENG (SA-TENG) was a typical example of electrostatically driven AC S-L TENG, which was developed by Yi et al. in 2016 [152] (Fig. 5e). It consisted of a conductive liquid electrode encapsulated within a rubber layer, exhibiting remarkable stretchability and flexibility. This design enabled the SA-TENG to maintain its electrical properties even under strains of up to 300%. By utilizing NaCl electrolyte, the SA-TENG significantly broadened its application potential. During operation, when the electropositive dielectric material contacted the electronegative rubber material, the electrons were induced to transfer from the ground to the conductive liquid. As the two dielectric materials were subsequently separated, the electrons in the conductive liquid returned to the ground. This process led to the generation of AC output. Experimental results indicated that the SA-TENG demonstrated a V_{OC} of approximately 67.71 V and an I_{SC} density of around 0.83 mA/m^2 in single-electrode mode (Fig. 5f and g), with its output performance significantly improving as the contact frequency and area increase. With its highly scalable manufacturing process, the SA-TENG was easily applicable for extensive energy harvesting. This method presented exciting opportunities for deformable and stretchable power sources, as well as self-powered sensors, making it suitable for a wide range of applications in fields such as soft robotics, biomechanics, physiology, and kinesiology. To further enhance the performance of electrostatically driven AC S-L TENGs, Luo et al. (2021) developed a single-electrode mode MXene/polyvinyl alcohol (PVA) hydrogel TENG (MH-TENG) [153] (Fig. 5h). By encapsulating the hydrogel within the silicon rubber Ecoflex, they effectively prevented water evaporation and leveraged the Ecoflex as a high-performance dielectric material. Simultaneously, the MXene/PVA hydrogel served as a conductive medium rich in ions, forming an EDL between the ecoflex and hydrogel. Through the dynamic modulation of the electrostatic field by the polyimide (PI), the system generated efficient AC output. Experimental

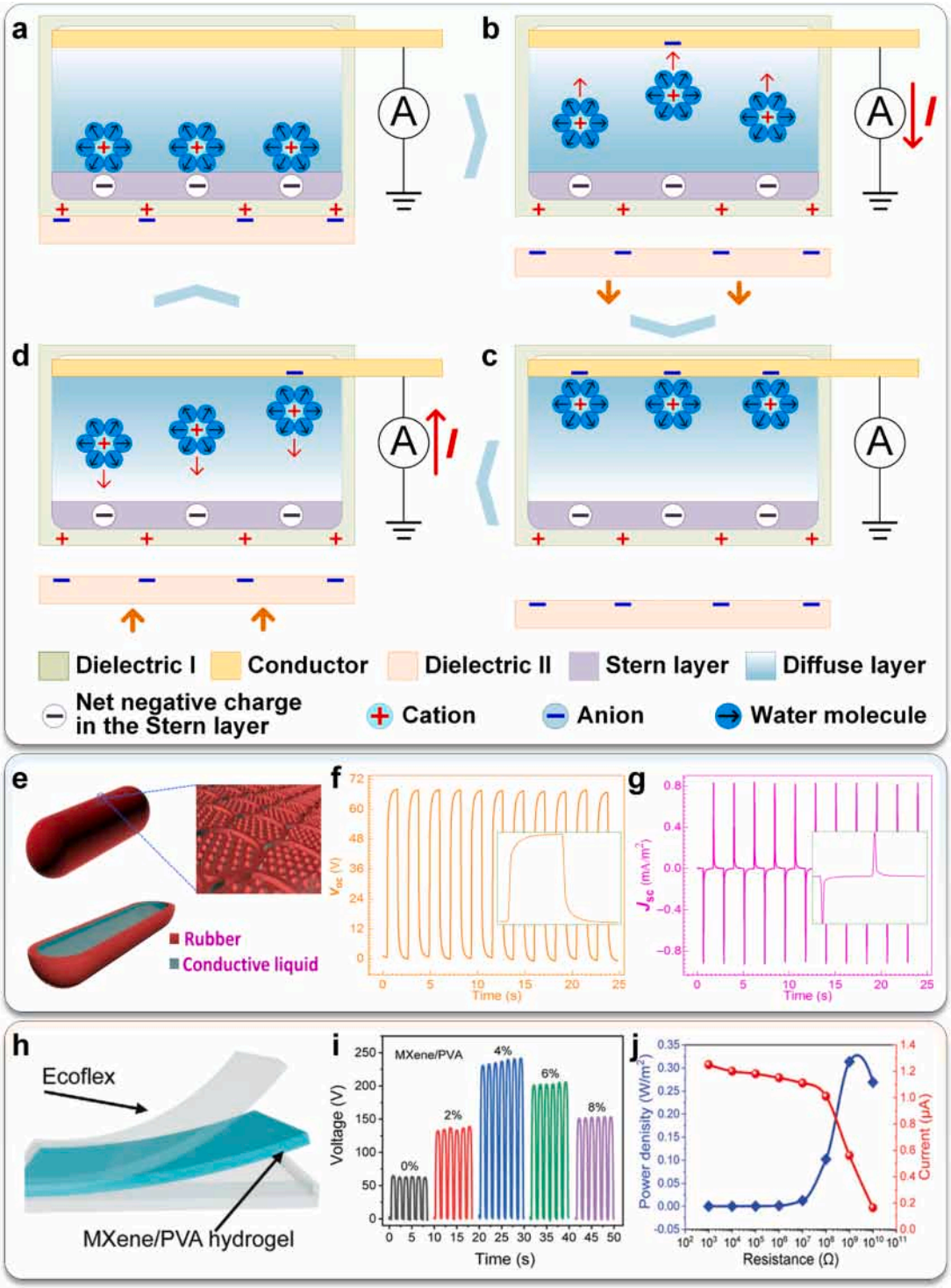

Fig. 5. The operating mechanism of electrostatically driven AC S-L TENGs and the output characteristics of typical devices. a–d, The operating mechanism of electrostatically driven AC S-L TENGs. e, The SA-TENG was developed by Yi et al. in 2016 [152]. f, Its V_{OC} was approximately 67.71 V. g, Its I_{SC} density was around 0.83 mA/m^2. h, The MH-TENG was developed by Luo et al. in 2021 [153]. i, Experimental results indicated that at an MXene doping concentration of 4%, the MH-TENG achieved optimal performance. j, The MH-TENG demonstrated an optimal power density of 0.33 W/m^2. e–g, Copyright 2016, The American Association for the Advancement of Science. h-j, Copyright 2021, WILEY-VCH.

results indicated that at an MXene doping concentration of 4%, the MH-TENG achieved optimal performance, exhibiting a V_{OC} of 230 V, an I_{SC} of 270 nA, and a Q_{SC} of 38 nC (Fig. 5i)–over four times greater than undoped PVA (60 V, 60 nA, 5 nC). This enhanced performance was attributed to the formation of microchannels in the hydrogel by MXene, which facilitated ion transport during the triboelectric process. However, at higher doping concentrations (8%), performance decreased due to the aggregation of MXene nanosheets, which impeded ion transport. The MH-TENG demonstrated an optimal power density of 0.33 W/m^2 (Fig. 5j), achieving efficient energy output. Beyond its impressive energy harvesting capabilities, the MH-TENG holds significant potential for applications in biomechanics, wearable devices, and

other advanced fields, marking a key advancement in the development of Electrostatically driven AC S-L TENGs for next-generation self--powered systems.

Overall, DC S-L TENGs could effectively generate constant current outputs that directly power electronic devices, addressing the limitations of rigid rectification systems that restrict their use in flexible applications. However, after the stable formation of the EDL, the output performance might be limited. S-L TENGs, which relied on the insulating properties of dielectric materials, typically exhibited higher internal resistance. While this elevated internal resistance facilitated the achievement of high-voltage outputs, enabling significant potential for applications in high-voltage domains, it simultaneously restricted

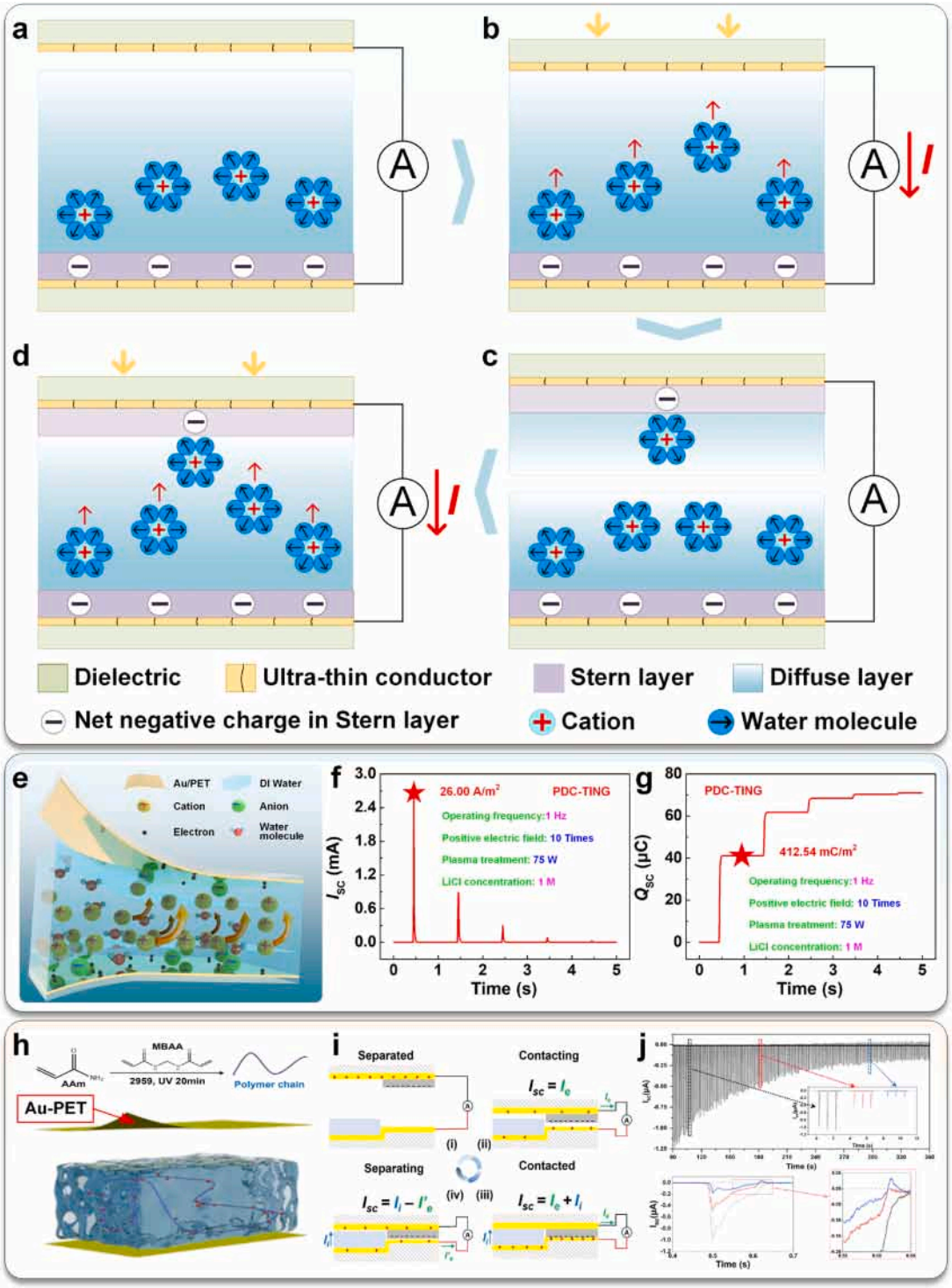

Fig. 6. The operating mechanism of TINGs via asymmetric EDLs and the output characteristics of typical devices. a–d, The operating mechanism of TINGs via asymmetric EDLs. e, In 2024, the PDC-TING was developed by Li et al. [96]. f, Its optimal output could reach an I_{SC} density of 26.00 A/m^2. g, The Q_{SC} density could reach to 412.54 mC/m^2. h, A TING using the PAAm hydrogel was constructed by Ouyang et al. in 2024 [154]. i, The ionic rectification mechanism of the TING via asymmetric EDLs. j, The generation and decay of the ionic current were closely related to the variations in electronic current. e–g, Copyright 2024, The Author(s). Distributed under the terms of the Creative Commons CC BY license. h–j, Copyright 2024, American Chemical Society.

current output. Therefore, it was crucial to strike a balance between voltage and current output in practical applications to optimize the performance of S-L TENGs, particularly in scenarios that demand higher power density. This balance was vital for enhancing their applicability in advanced technologies, including flexible electronics, wearable devices, and renewable energy systems.

4. Various types of TINGs

TINGs have demonstrated the capability to generate effective pulsed DC outputs through two primary mechanisms: the creation of asymmetric EDLs at ultra-thin conductor-liquid interfaces on dielectric substrates, and the precise regulation of charge density within the diffuse layer of the EDL close to dielectric surfaces. These strategies enabled efficient charge dynamics and dynamic modulation of ionic and electronic behaviors at the interface. In addition to achieving enhanced harvesting for energy applications, recent advancements have explored the integration of a bidirectional electrostatic field, induced by S-S CE, to dynamically regulate the charge distribution within the EDL. This innovative approach facilitated a seamless combination of energy harvesting and information transmission, leveraging the EDL's inherent responsiveness to external stimuli. These attributes highlighted their extensive application prospects, ranging from autonomous energy systems to advanced sensing technologies and smart interface controls, offering transformative solutions for sustainable energy and next-generation intelligent devices.

4.1. TINGs based on asymmetric EDLs

To effectively enhance the current output of nanogenerators, TINGs were developed. These devices could generate effective pulsed DC outputs through two primary mechanisms: by creating asymmetric EDLs at the ultra-thin conductor-liquid interface on dielectric substrates, or by replenishing the charge density in the EDLs adjacent to dielectric surfaces. These innovations allowed for improved Q_{SC} and P_R densities, making TINGs a promising solution for various applications requiring reliable and efficient power sources. The TING based on asymmetric EDLs exhibited a unique operational mechanism that efficiently enhanced Q_{SC} density. This device was primarily composed of a hybrid material that integrated a dielectric substrate with a closely adhered ultra-thin conductive layer (Fig. 6a). The ultra-thin conductive layer could serve not only as a charge-collecting layer but also as a means to adjust the substrate-liquid CE properties, thereby regulating the EDL. Upon contact between the liquid and the bottom hybrid material, the liquid infiltrated through the micro-cracks in the ultra-thin metallic layer, establishing a direct interface with the dielectric substrate, which facilitated the formation of an EDL. As the upper hybrid material made contact with the liquid, a new EDL was formed, creating two EDLs with different symmetries (Fig. 6b). This configuration created an ion concentration gradient that enhanced ionic migration, thereby facilitating electron transfer within the external circuit and generating an ionic current. When the upper hybrid material was lifted away from the liquid, ion migration was temporarily interrupted (Fig. 6c). Through continuous cycles of contact and separation, the ion concentration gradient diminished over time, and ion migration persisted until equilibrium was achieved between the two EDLs (Fig. 6d). This innovative mechanism not only improved the efficiency of Q_{SC} but also underscored the potential of TINGs in various energy harvesting applications, highlighting their ability to convert mechanical energy into electrical energy effectively.

In 2024, the physically adsorptive direct-current TING (PDC-TING) based on asymmetric EDLs was developed by Li et al. [96] (Fig. 6e), which used polyethylene terephthalate (PET) as the dielectric substrate with an ultrathin gold (Au) layer deposited via magnetron sputtering. To effectively enhance the output performance of the PDC-TING, three strategies were proposed to increase the ion concentration gradient. Firstly, by adjusting the electrostatic fields, positive and negative electric fields were established on polyamide (PA) and PTFE films, respectively. The positive electric field facilitated the formation of asymmetric EDLs and the migration of ions, thereby improving the output current, while the negative field resulted in a decrease in output current. Secondly, plasma treatment was employed to enhance the hydrophilicity of the bottom hybrid material (Au/PET), significantly increasing the density of the bottom EDL and, consequently, the ion concentration gradient. Lastly, replacing the water with various concentrations of LiCl solution not only augmented the EDL density but also reduced internal resistance by increasing ion concentration, thereby minimizing energy losses and enhancing signal strength and sensitivity. Collectively, these strategies contributed to the overall performance improvement of the PDC-TING. Its optimal output could reach an I_{SC} density of 26.00 A/m^2 (Fig. 6f), a Q_{SC} of 41.25 μC, and a P_R of 0.85 mW, corresponding to a Q_{SC} density of 412.54 mC/m^2 (Fig. 6g) and a P_R density of 8.45 W/m^2. This higher Q_{SC} density was essential for improving energy output efficiency and enhancing signal strength and sensitivity in TENGs. Increased charge density enabled the collection of more charge per contact, resulting in a more stable power source for self-powered devices in the energy flow field. In the information flow field, elevated charge transfer density boosted signal strength and detection sensitivity, allowing for greater precision and rapid response in monitoring subtle physical changes or environmental conditions. Consequently, the PDC-TENG demonstrated significant potential for applications in both energy harvesting and high-sensitivity sensing. Furthermore, TENGs based on asymmetric EDLs could generate ionic currents that facilitated ionic rectification, thereby modulating conventional AC TENGs to generate the DC ionic-electronic couple output. In 2024, Ouyang et al. successfully constructed a TING using polyacrylamide (PAAm) hydrogel [154] (Fig. 6h), achieving rectification of AC TENG outputs. The hydrogel was synthesized by injecting a reagent solution into a custom mold and initiating polymerization with ultraviolet light. Subsequently, it was placed on the surface of the bottom hybrid material (PET substrate and its surface sputtered ultra-thin Au layer). The study revealed that the interaction between ionic and electronic currents allows the ionic current to flow in the same direction as the electronic current when the composite material was in proximity to the hydrogel, while it offseted the electronic current during separation (Fig. 6i). This mechanism validated the effectiveness of ionic rectification. Experimental results demonstrated that the generation and decay of the ionic current were closely related to the variations in electronic current, underscoring the importance of ionic current in enhancing energy output efficiency and rectification performance (Fig. 6j). This flexible ionic rectification mechanism overcame the limitations of conventional rigid rectifiers, offering enhanced adaptability, lightweight design, and improved energy output efficiency, paving the way for new opportunities in wearable devices and flexible electronics.

4.2. TINGs based on regulating charge density of the diffuse layer

In addition to achieving higher Q_{SC} density by TINGs based on asymmetric EDLs, regulating the charge density of the diffuse layer close to the dielectric material could also create an ion concentration gradient that drives effective ionic migration. This adjustment could also modulate the AC electronic displacement current generated by the TENG, resulting in higher power density DC ionic-electronic coupling output. The working principle was as follows: when the water contacted the dielectric material surface, an EDL was formed (Fig. 7a). By spraying pre-charged positive water mist generated by S-L CE onto the dielectric surface, the charge density of cations in the diffuse layer could be dynamically adjusted, establishing an ion concentration gradient. As the bottom electrode contacted the water on the dielectric surface, cations migrated to the electrode surface, generating an efficient ionic current in the external circuit (Fig. 7b). The contact between the bottom electrode and the dielectric surface expelled the water. Due to differences in

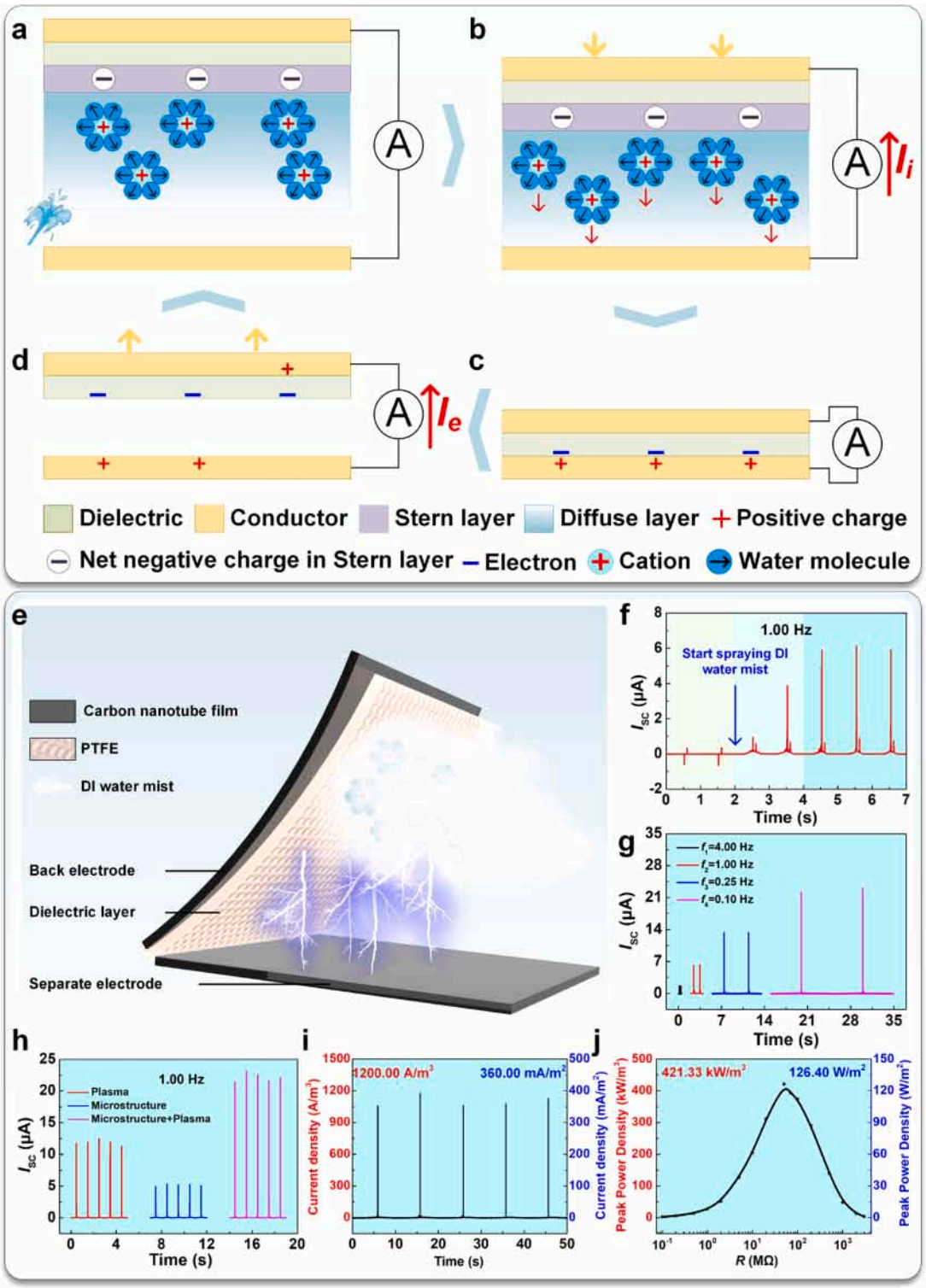

Fig. 7. The operating mechanism of the TING via regulating charge density of the diffuse layer and the output characteristics of the higher-power density DC TING. a–d, The operating mechanism of the TING via regulating charge density of the diffuse layer. e, In 2023, the higher-power density DC TING was developed by Li et al. [95]. f, The principle verification experiment of the DC-TING. g, The influence of operating frequency on the output performance. h, The influence of the hydrophilic area of the dielectric layer on the output performance. i, Its I_{SC} density could reach 360.00 mA/m^2. j, Its P_R density could reach 126.40 W/m^2. e-j, Copyright 2023, Elsevier Inc.

electronegativity, electrons from the bottom electrode were transferred to the dielectric surface (Fig. 7c). Upon separation of the electrodes, electrons transferred from the top electrode to the bottom electrode based on the principle of electrostatic induction, creating an electronic displacement current in the external circuit (Fig. 7d). The ionic current flowed in the same direction as the electronic displacement current, resulting in DC output. This mechanism enabled stable energy output by continuously regulating the charge density of the diffuse layer through the spraying of pre-charged water mist.

In 2023, a higher-power density DC TING based on regulating the

charge density of the diffuse layer was developed by Li et al. [95] (Fig. 7e), which utilized PTFE as the dielectric material and carbon nanotubes as electrode materials. This innovative design, featuring carbon nanotube film electrodes, significantly enhanced ionic charge-collecting efficiency and environmental stability. Initial experiments demonstrated that in a dry state, without spraying water mist, the DC-TING functioned as a conventional TENG, generating approximately AC I_{SC} of 0.8 μA (Fig. 7f). However, upon spraying pre-charged deionized water, the DC I_{SC} increased to around 6.0 μA, showcasing the device's capacity for effective DC output through adjustments in the charge density of the diffuse layer in the EDL close to the dielectric layer. The study further revealed that reducing the operating frequency from 4.00 Hz to 0.10 Hz significantly improved output performance (Fig. 7g). This enhancement was attributed to the extended charge replenishment time, which allowed a greater amount of pre-charged water to accumulate ions in the diffuse layer on the dielectric surface, thereby increasing both current and power output. Additionally, the research explored the impact of increasing the hydrophilic area of the dielectric layer on DC-TING output (Fig. 7h). Modifications to the PTFE film—achieved through the method of plasma sputtering after micro--engraving—resulted in improved hydrophilicity. This increased contact area with pre-charged water enhanced ionic charge storage capacity and transfer efficiency, facilitating the formation of a denser diffuse layer. As a result of these advancements, the DC-TING achieved significant enhancements in key performance metrics at 0.10 Hz, with I_{SC} reaching 36.0 μA, Q_{SC} of 560.0 nC, V_{OC} of 1750 V, and P_R output of 12.64 mW. Calculations indicated an ultra-high I_{SC} density of 360.00 mA/m^2 (Fig. 7i), along with a Q_{SC} density of 5.60 mC/m^2, and a P_R density of 126.40 W/m^2 (Fig. 7j). These findings underscored the effective energy output capabilities of the DC-TING system, highlighting its potential for various applications in energy harvesting and self-powered devices.

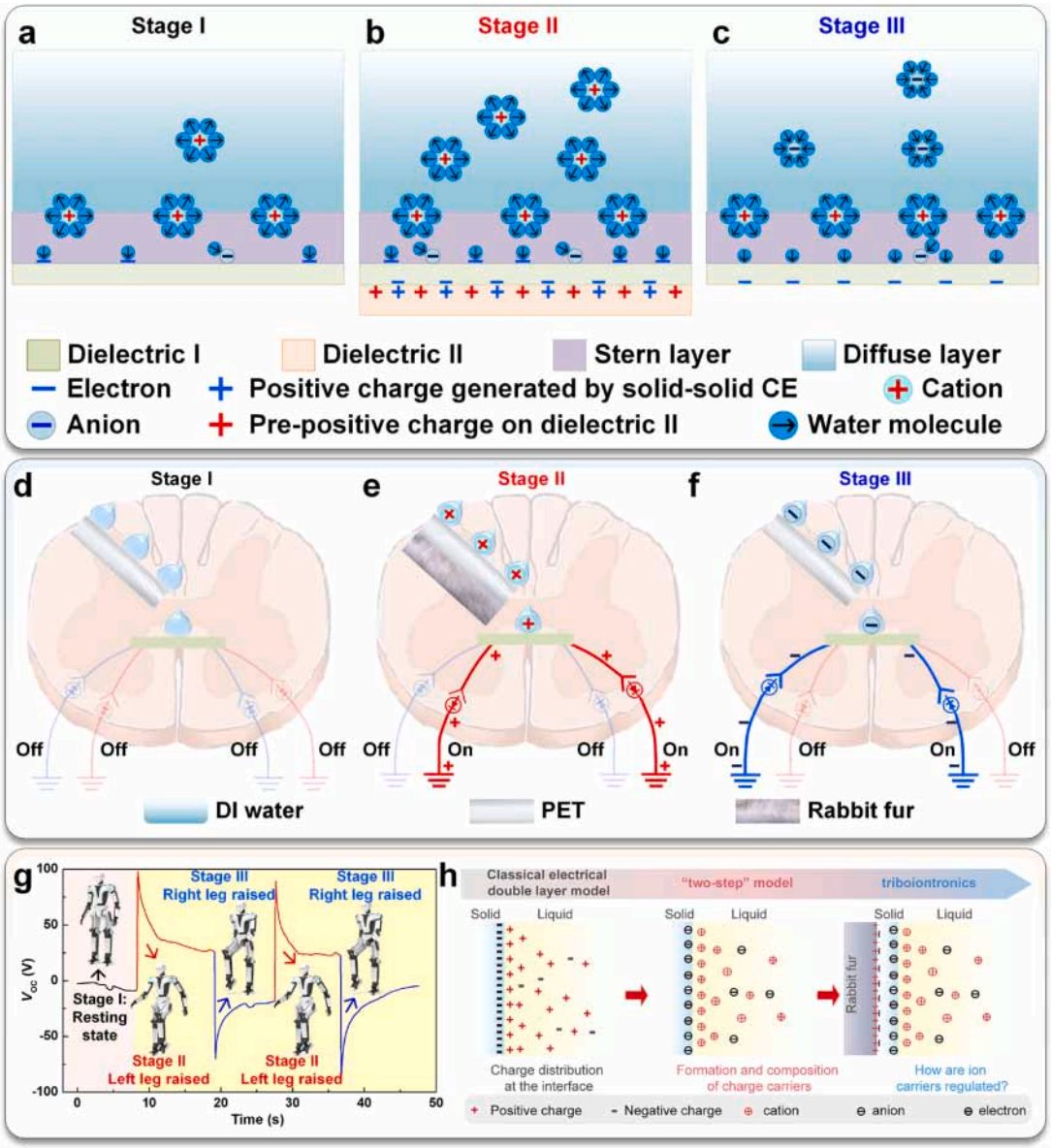

Fig. 8. The triboiontronic bionic neurologic circuit via dynamically adjusting the charge distribution of the EDL. a–c, Utilizing S-S CE could effectively regulate the charge distribution within the EDL, thereby modulating the ionic charge polarity in the diffuse layer. d–f, The operating mechanism of the triboiontronic bionic neurologic circuit via dynamically adjusting the charge distribution of the EDL [95]. g, By modifying the contact states between the rabbit fur and the PET sprayer, the water with different ionic charge polarities directly governed the robot's rhythmic and coordinated movements. h, In 2023, Wang et al. highly praised the concept of "triboiontronics" proposed by Wei et al. [155]. d–g, Copyright 2023, Elsevier Inc. h, Copyright 2023, Elsevier Inc.

4.3. Triboiontronic bionic neurologic circuit via dynamically regulating the charge distribution of the EDL

In addition to achieving higher Q_{SC} or P_R density in energy applications with TINGs, research has also explored the generation of a bidirectional electrostatic field through S-S CE to modulate the charge distribution of the EDL. This adjustment influenced the polarity of ionic charges in the diffuse layer, enabling the construction of the triboiontronic bionic neurologic circuit. It could transmit the physical contact information generated during the S-S CE process, store the ionic charge polarity information within the diffuse layer, and ultimately convert this data into the corresponding electronic signal. In Stage I (Fig. 8a), when the water contacted the PET film, a negatively charged Stern layer was formed, resulting in a weaker positive charge in the diffuse layer. In Stage II (Fig. 8b), upon introducing positively charged rabbit fur based on pre-CE on the backside of the PET film, the electronegativity difference caused electrons to transfer from the fur to the PET film. The pre-charged positive charge on the fur induced an electrostatic attraction that draws anions from the water toward the S-L contact interface. This migration enhanced the release of cations in the diffuse layer, resulting in an increased ionic concentration. In Stage III (Fig. 8c), once the rabbit fur was removed, the retained electrons on the PET surface created a negative electric field, attracting cations toward the S-L contact interface. However, the high hydration energy of these cations prevented them from escaping their hydration shells to directly adsorb on the PET surface. Consequently, the IHP remained largely comprised of the dipole layer of water molecules, while hydrated cations formed the OHP, resulting in a positively charged Stern layer. At this stage, a significant number of anions remained freely available in the diffuse layer. Therefore, utilizing S-S CE could effectively regulate the charge distribution within the EDL, thereby modulating the ionic charge polarity in the diffuse layer.

The described dynamic regulation mimics the straightforward control of a neurological circuit, facilitating the development of the triboiontronic bionic neural circuit [95]. In this bionic circuit, the interaction between charged materials and the EDL enabled the modulation of electronic currents across three distinct stages. In Stage I (Fig. 8d), the water was applied to a PET film while the positively charged rabbit fur remained at a distance, resulting in the external circuits being in a disconnected state, analogous to a resting condition. Stage II began when the pre-positive charged rabbit fur made contact with the PET film (Fig. 8e). This contact led to an induction effect, where the positively charged diffuse layer in the water prompted a forward electronic current in the external circuits, as indicated by red highlights. In Stage III (Fig. 8f), the removal of the rabbit fur altered the system's charge dynamics. The negatively charged diffuse layer in the water then induced a reverse electronic current, represented in blue. This shift occurred because the retained negative charges on the PET film attract positive ions from the water, leading to a change in the current direction. So, in this bionic circuit, the ionic charge polarity of the diffuse layer can be adjusted through simple S-S CE, enabling the transfer of perceived physical contact information and the coordinated generation of bidirectional electronic currents without the need for an external power source. The EDL not only facilitated information transmission but also achieved rhythmic alternating control of induced bidirectional electronic currents, paralleling the functions of biological neurological circuits (Fig. 8g). In Stage I, the bionic circuit was resting, immobilizing the virtual robot. In Stages II and III, by modifying the contact states between the rabbit fur and the PET sprayer, the water with different ionic charge polarities directly governed the robot's rhythmic and coordinated movements. Ionic-electronic coupling in this triboiontronic bionic neurologic circuit provided a simple, safe, and efficient interface for human-computer interaction, without the need for external power. When integrated with distributed parallel processing and high biocompatibility, this technology can support self-powered in-sensor computing systems, implantable neuronal-computer interfaces, and low-power neuromorphic devices, enabling a range of advanced functionalities. In 2023, Wang et al. authored a dedicated preview of the concept of "triboiontronics" introduced by Wei et al., in Matter [155] (Fig. 8h), emphasizing its innovative approach to dynamically regulating ion carriers in the EDL through CE. This strategy facilitates an efficient integration of energy harvesting and information transmission. They noted that the developed DC-TING significantly enhanced power density, overcoming the limitations of traditional devices. Overall, TINGs were expected to attract greater research interest for their potential in efficient energy harvesting, precise control of interfacial EDLs, and rapid regulation of biomimetic nervous systems, showcasing broad application prospects.

5. Hydrovoltaic technology

By creating asymmetric EDLs at ultra-thin conductor-liquid interfaces on dielectric substrates, TENGs have achieved effective pulsed DC outputs through dynamic charge separation and redistribution. In contrast, hydrovoltaic technology leveraged similar ultra-thin conductor-liquid interfaces but focused on the mechanical manipulation of the EDL boundary to produce stable constant outputs. This stability made hydrovoltaic technology particularly advantageous for sustained energy applications, as they were designed to harness continuous ion migration and concentration gradient for reliable power generation. When a droplet was deposited on the ultra-thin conductor layer of a dielectric substrate, the liquid directly contacted the dielectric substrate through the microscopic cracks in the conductor, forming a stable DL (Fig. 9a). As the droplet began to slide, the liquid at the front extended and contacted the solid material, creating a new EDL. This resulted in an ionic concentration gradient between the front and rear ends of the droplet, driving the migration of cations toward the front, which in turn causes electrons to flow in the circuit, generating an electric current (Fig. 9b). In 2014, Yin et al. developed hydrovoltaic technology by driving droplets to slide on a monolayer graphene surface on a PET substrate [144] (Fig. 9c). In the experiment, droplets of 0.6 M NaCl aqueous solution were sandwiched between the graphene/PET surface and a 5×5 mm^2 SiO_2/Si wafer, which moved along a fixed track, allowing the droplets to slide on the graphene. By adjusting the sliding speed of the droplets, a voltage signal was generated that was linearly correlated with the speed, increasing from 0.09 mV at 1.3 cm/s to 0.59 mV at 8.55 cm/s. Furthermore, when the droplets moved in a triangular wave pattern, the V_{OC} signal accurately reflected their speed changes, while sinusoidal motion produced a corresponding sine-wave voltage response (Fig. 9d). These results indicated the potential applications of graphene in liquid motion monitoring. Additionally, when multiple droplets moved simultaneously, the voltage output was proportional to the number of droplets; for example, three droplets sliding in tandem at 8.55 cm/s could produce nearly 2 mV of V_{OC} (Fig. 9e). It was also observed that when two droplets moved in opposite directions on the same graphene sheet, the voltages generated by each droplet would cancel each other out. This demonstrated that the direction of ion migration, regulated by the movement of the EDL boundary, was critical in determining the direction of the generated current.

In 2018, Yang et al. conducted sum frequency generation vibrational spectroscopy (SFVS) experiments to investigate the mechanisms and influencing factors of hydrovoltaic technology at the molecular level [145] (Fig. 9f), focusing on the structural and charge transfer behavior at the dielectric-liquid and graphene/dielectric-liquid interfaces. The experiments revealed that PET surfaces can generate a surface electric field, which significantly increases in intensity with rising salt concentration (Fig. 9g). In contrast, such a field was not observed at the poly methyl methacrylate (PMMA) interface, as the spectra at the water/-PMMA interface remained unchanged with varying salt concentrations, indicating a nearly neutral surface. This suggests that neither PMMA nor graphene significantly attracts ions. On the other hand, the spectral intensity at the PET interface showed a marked increase with increasing

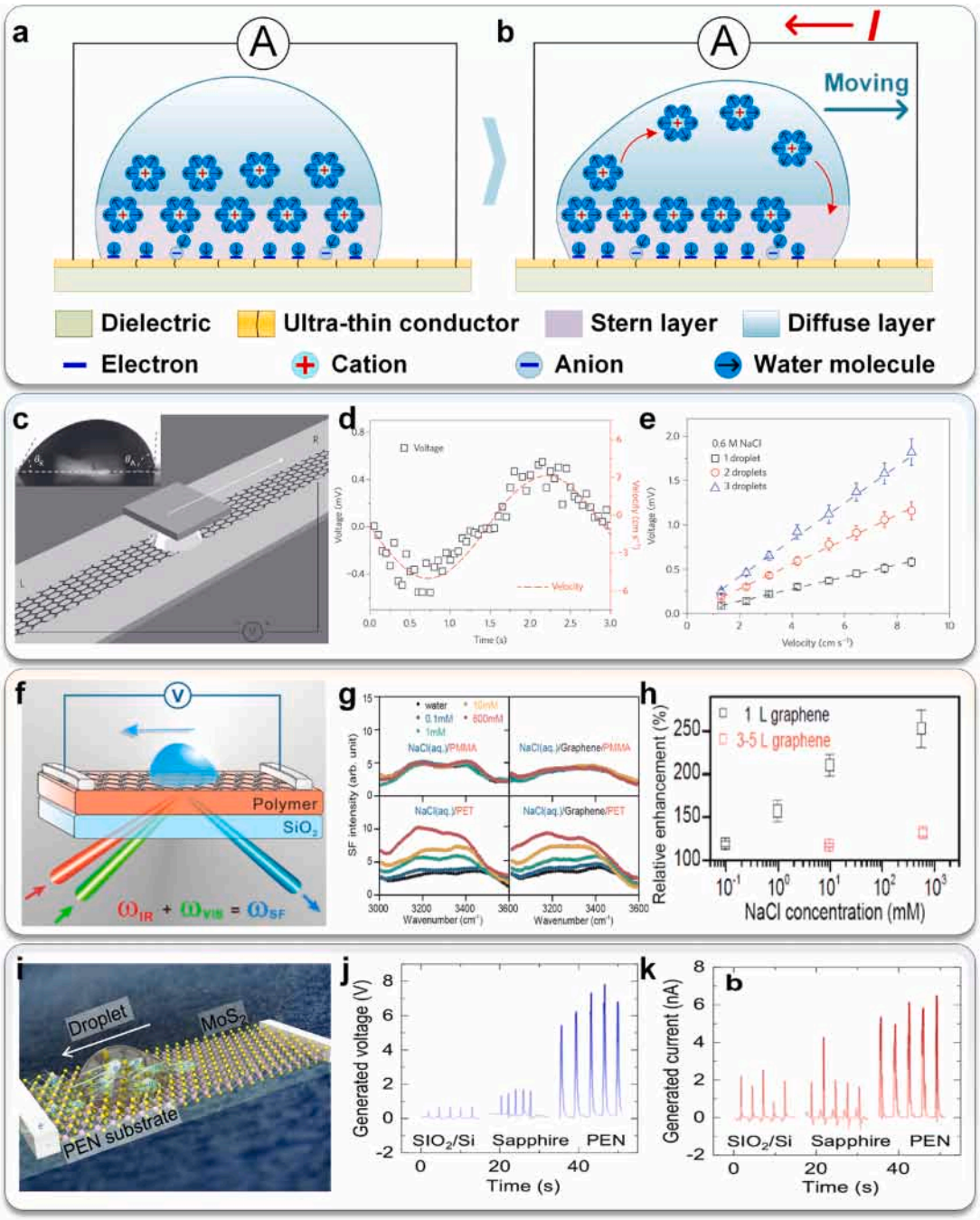

Fig. 9. The operating mechanism of hydrovoltaic technology and the output characteristics of its typical devices. a, b, The operating mechanism of the hydrovoltaic technology. c, In 2014, a typically hydrovoltaic technology device was developed by Yin et al. [144]. d, By adjusting the sliding speed of the droplets, the V_{OC} was generated that was linearly correlated with the speed. e, When multiple droplets moved simultaneously, the voltage output was proportional to the number of droplets. f, In 2018, the SFVS experiment was conducted by Yang et al. to investigate the mechanisms and influencing factors of hydrovoltaic technology [145]. g, The charge transfer of the hydrovoltaic technology was primarily based on the properties of the dielectric substrate. h, The ultrathin conductive layer serves solely as a charge-collecting layer, providing a screeding effect on the charge transfer between the dielectric substrate and the liquid. i, In 2020, a hydrovoltaic technology device via the MoS_2 film was developed by Aji et al. [156]. j, The V_{OC} could reach 8 V. k, The I_{SC} could reach 6 nA. c–e, Copyright 2014, Springer Nature Limited. f-h, Copyright 2018, American Chemical Society. i-k, Copyright 2019, Elsevier Ltd.

salt concentration, indicating that Na^+ ions migrated to the interface, perturbing the water structure. Additionally, the spectral intensity at the water/graphene/PET interface was slightly lower than that of the water/PET interface, suggesting that monolayer graphene has a certain screening effect on the surface electric field. This experiment demonstrated that the formation of the EDL in hydrovoltaic technology is based on charge transfer between the dielectric substrate and the liquid. The ultrathin conductive layer on the dielectric substrate, such as monolayer graphene, primarily acts as a charge collection layer but exerts a partial screening effect on the formation of the EDL. As further validation, increasing the number of graphene layers led to a gradual reduction in hydrovoltaic technology (Fig. 9h), confirming that the thicker the conductive layer, the stronger the screening effect. In hydrovoltaic technology, the use of monolayer graphene as an ultrathin conductive layer resulted in lower V_{OC} due to its excellent conductivity, which affected its ability to power electronic devices. To address this issue,

semiconductor materials could be employed as the ultrathin conductive layer. The increased internal resistance of semiconductors helped to effectively enhance the voltage output, potentially improving the power supply for electronic applications. In 2020, Aji et al. developed large-area monolayer molybdenum disulfide (MoS_2) films on a polyethylene naphthalene (PEN) substrate [156] (Fig. 9i). By driving liquid motion across the surface of these films, they were able to generate a significantly high output voltage. This study systematically investigated the performance of MoS_2 nanogenerators on different substrates (PEN, sapphire, and SiO_2/Si) to assess the impact of substrate material on power output. Electricity generation was triggered by depositing 50 μL of a 1 M NaCl solution onto the surface of MoS_2 films laid on different substrates. The results demonstrated that the MoS_2/PEN device achieved the highest V_{OC} of 8 V (Fig. 9j) and I_{SC} of 6 nA (Fig. 9k), outperforming devices on other substrates. These findings further validated the significant influence of substrate material on output performance and suggested that increasing the sheet resistance of ultrathin conductive materials could effectively enhance V_{OC}, thus optimizing energy

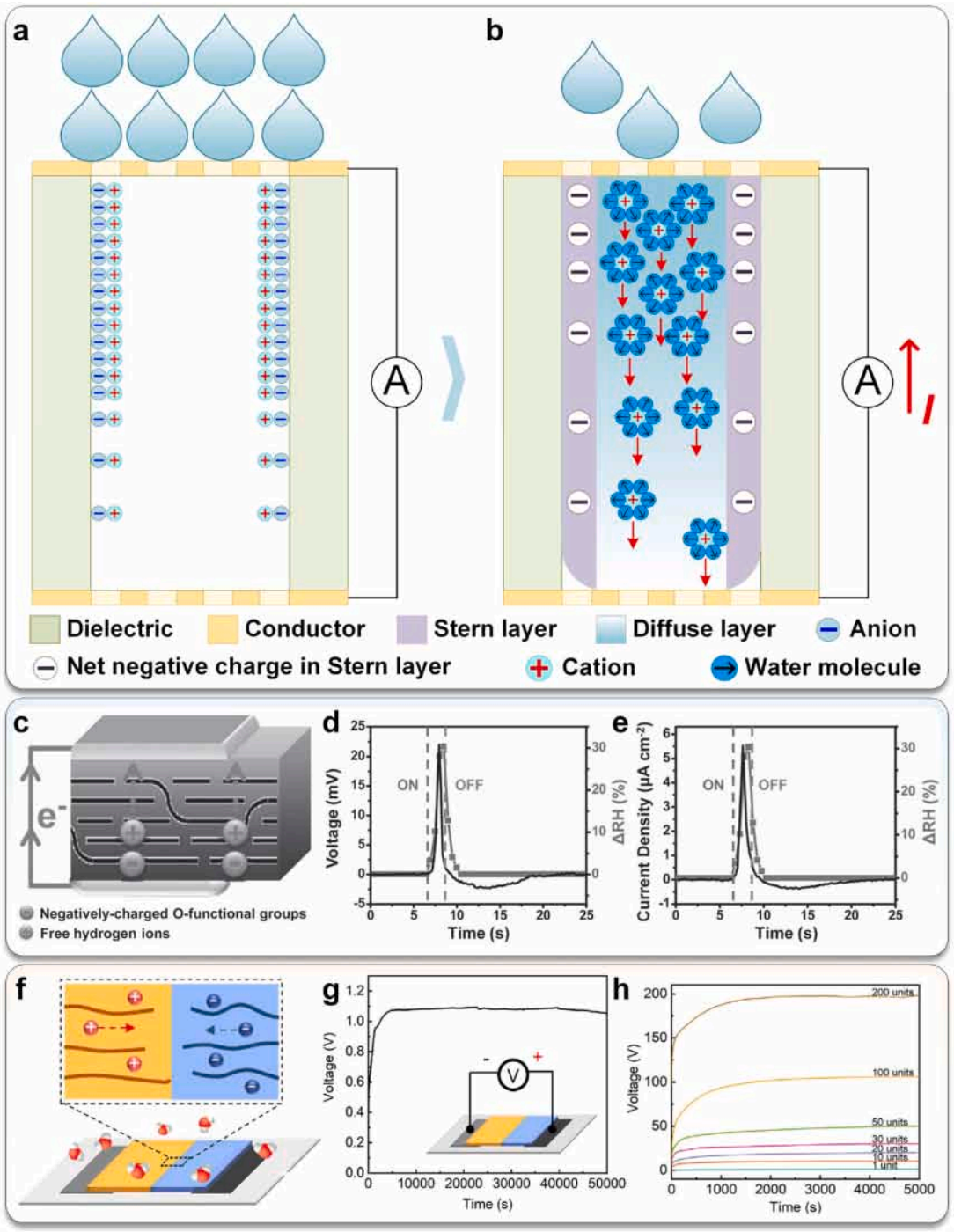

Fig. 10. The operating mechanism of MEGs based on humidity-induced functional group hydrolysis and the output characteristics of its typical devices. a, b, The operating mechanism of MEGs based on humidity-induced functional group hydrolysis. c, A typical MEG utilizing a GO film was developed by Zhao et al. in 2015 [157]. d, e, As humidity increased, the induced positive V_{OC} and I_{SC} rose sharply, reaching peak values of 22 mV and 5.5 μA/cm^2. f, The PMEG that achieved significant voltage output was developed by He et al. in 2023 [146]. g, A single PMEG could generate a V_{OC} of up to 1.1 V. h, When 200 PMEG units were connected in series, they could achieve a V_{OC} of 200 V. c-e, Copyright 2015, WILEY-VCH Verlag GmbH & Co. KGaA. f-h, Copyright 2023, Elsevier Inc.

generation.

6. Various types of MEGs

Hydrovoltaic technology could generate a constant current output by dynamically regulating the EDL boundary. While mechanical drive was one possible method to induce this movement, other mechanisms, such as fluid flow or ionic diffusion, can also achieve this effect. In contrast, MEGs enabled directional ion migration within the Debye length of the EDL through two primary mechanisms: humidity-induced hydrolysis of functional groups, which created an ion concentration gradient, and evaporation-driven transport of specific polar ions through charged ion channels. These processes allowed MEGs to produce constant current output without requiring continuous external mechanical drive, offering a more efficient and convenient approach to energy harvesting.

6.1. MEGs based on humidity-induced functional group hydrolysis

In MEGs that operated based on humidity-induced functional group hydrolysis, numerous oxygen-containing groups (e.g., -OH, -COOH) were grafted onto the inner wall of one end of the ion channel (Fig. 10a). These groups exhibited a gradient distribution and strong hydrophilicity. When exposed to moisture, water molecules were adsorbed at the oxygen-rich region of the channel. As the water accumulates, the solvation effect could weaken the $O\delta^{-}-H\delta^{+}$ bonds within these oxygen-containing groups, releasing free cations. This contributed to the formation of the EDL and created a concentration gradient of H^{+} ions (Fig. 10b). Once the cations migrated within the Debye length range along the ion channel, driven by the concentration gradient, an induced potential was generated in the external circuit, leading to the electron transfer in an external circuit. This characteristic facilitated sustained energy production without relying on external mechanical systems. By harnessing environmental moisture and the associated ionic movement, these devices could achieve stable and uninterrupted electrical output, making them particularly advantageous for applications requiring consistent power supply.

Graphene oxide (GO), serving as a precursor and support matrix for synthesizing graphene-based composite materials, exhibits excellent functionalization capabilities and controllability. When compounded with metals, metal oxides, and polymer materials, GO provides a large specific surface area, effectively dispersing and adhering to substrates, thus preventing aggregation. Notably, due to its outstanding proton conductivity and permeability to water, GO has emerged as a critical material for efficient power sources. In 2015, Wei developed a highly efficient sketchable planar power source using GO [158], offering a safe energy solution that enables new applications difficult to achieve with traditional battery technology, including the construction of foldable energy systems on paper and platforms for future wearable electronic devices. In addition, GO could also hold significant potential in the field of MEGs. Zhao et al. developed a typical MEG utilizing the GO film [157] (Fig. 10c). In this MEG, the GO film functioned as both the dielectric and functional layer. When exposed to moisture (at 30% relative humidity), the oxygen-containing functional groups on the GO film underwent hydrolysis, leading to the formation of a hydrogen ion concentration gradient. This gradient drove ion migration, resulting in observable current conduction in the external circuit. This process emphasized the critical role of GO in facilitating moisture-induced charge transfer, a key mechanism for energy generation in MEG systems. When the environmental humidity returned to its initial level, ions migrated back due to the reverse concentration gradient, producing a reverse current signal with a negative voltage. As a result, the device reverted to its original state, completing a full operational cycle. The study also examined the distinct single-cycle output behavior as relative humidity fluctuated. As humidity increased, the induced positive V_{OC} and I_{SC} rose sharply, reaching peak values of 22 mV (Fig. 10d) and 5.5 μA/cm^2 (Fig. 10e), respectively, before returning to zero as the humidity stabilized. During the decrease in humidity, the voltage shifted negatively and persisted for several seconds after the moisture was fully removed. This observation suggested that the power generation mechanism is directly tied to the interaction between water molecules and the GO framework. To further enhance the output performance of MEGs, a bidirectional ion migration approach involving the coupling of both cations and anions can be adopted. This method allows for more efficient ion transport, optimizing the energy conversion process and improving the overall performance of the MEG system. In 2023, He et al. developed a fully printed MEG (PMEG) that achieved significant voltage output [146] (Fig. 10f). The PMEG unit comprised polystyrene sulfonic acid (PSSA), polydiallyl dimethyl ammonium chloride (PDDA), and a pair of asymmetric electrodes. The positive electrode was a carbon electrode located on the PDDA side, while the negative electrode was a carbon-aluminum composite electrode on the PSSA side. Both PSSA and PDDA, as electrolyte gels, dissociated mobile H^{+} and Cl^{-} ions upon moisture absorption. The incorporation of active aluminum in the negative electrode on the PSSA side enhanced the performance of the generator. The Al reacts with H^{+} ions, significantly improving the output voltage. This design took advantage of the dissociation and mobility of ions in the electrolyte gel and the reactivity of aluminum, resulting in enhanced voltage output and marking a notable improvement in the efficiency of moisture-induced energy generation systems. A single PMEG with an area of 0.3 cm^2 could generate a V_{OC} of up to 1.1 V (Fig. 10g) and a power density of 2.6 mW/cm^2 under conditions of 80% relative humidity. By customizing screen patterns, it was possible to print hundreds to thousands of PMEG units on various substrates and connect them in series or parallel configurations. For instance, when 200 PMEG units were connected in series, they could achieve a V_{OC} of 200 V (Fig. 10h).

6.2. MEGs based on evaporation-driven transport of specific polar ions

Once the functional groups underwent complete hydrolysis, MEGs relying on humidity-induced functional group hydrolysis lost their capacity to maintain a stable ion concentration gradient. This deficiency led to a substantial decrease in ion migration, resulting in a significant decline in output performance. The reduction in performance could be attributed to the depletion of reactive sites necessary for the ongoing generation of charge carriers, which impeded sustained energy production. To tackle this challenge, an alternative mechanism that leveraged liquid evaporation was implemented. This process facilitates the movement of specific polar ions through ion channels that acquire distinct charges due to the complete hydrolysis of functional groups. Consequently, MEGs that utilized evaporation-driven transport of these specific polar ions could maintain a stable and continuous constant current output. Initially, after the functional groups had fully hydrolyzed, the inner walls of the ion channels developed a stable EDL characterized by specific net charges (Fig. 11a). When these charged ion channels were immersed in a liquid, the evaporation process initiated fluid flow through the nanochannels. Throughout this mechanism, the EDL promoted the continuous migration of ions with opposite polarity within the Debye length, while effectively obstructing the entry of ions with the same polarity (Fig. 11b). This innovative approach significantly enhanced the functionality of the MEGs based on the evaporation-driven transport of specific polar ions by enabling a more reliable and efficient ion transport process. As a result, the device could consistently generate stable constant current output, making it a promising candidate for various energy applications.

In 2017, a typical MEG based on evaporation-driven transport of specific polar ions was developed by Ding et al. [124] (Fig. 11c), which was inspired by the energy-harvesting mechanisms observed in trees. The working principle relied on the evaporation of water, which drove specific polar ions to migrate through the EDL along the surfaces of nanochannels, generating an electric current. Experimental results demonstrated that the MEG could produce a V_{OC} of up to 1 V in an ambient environment with a relative humidity of 62% and could

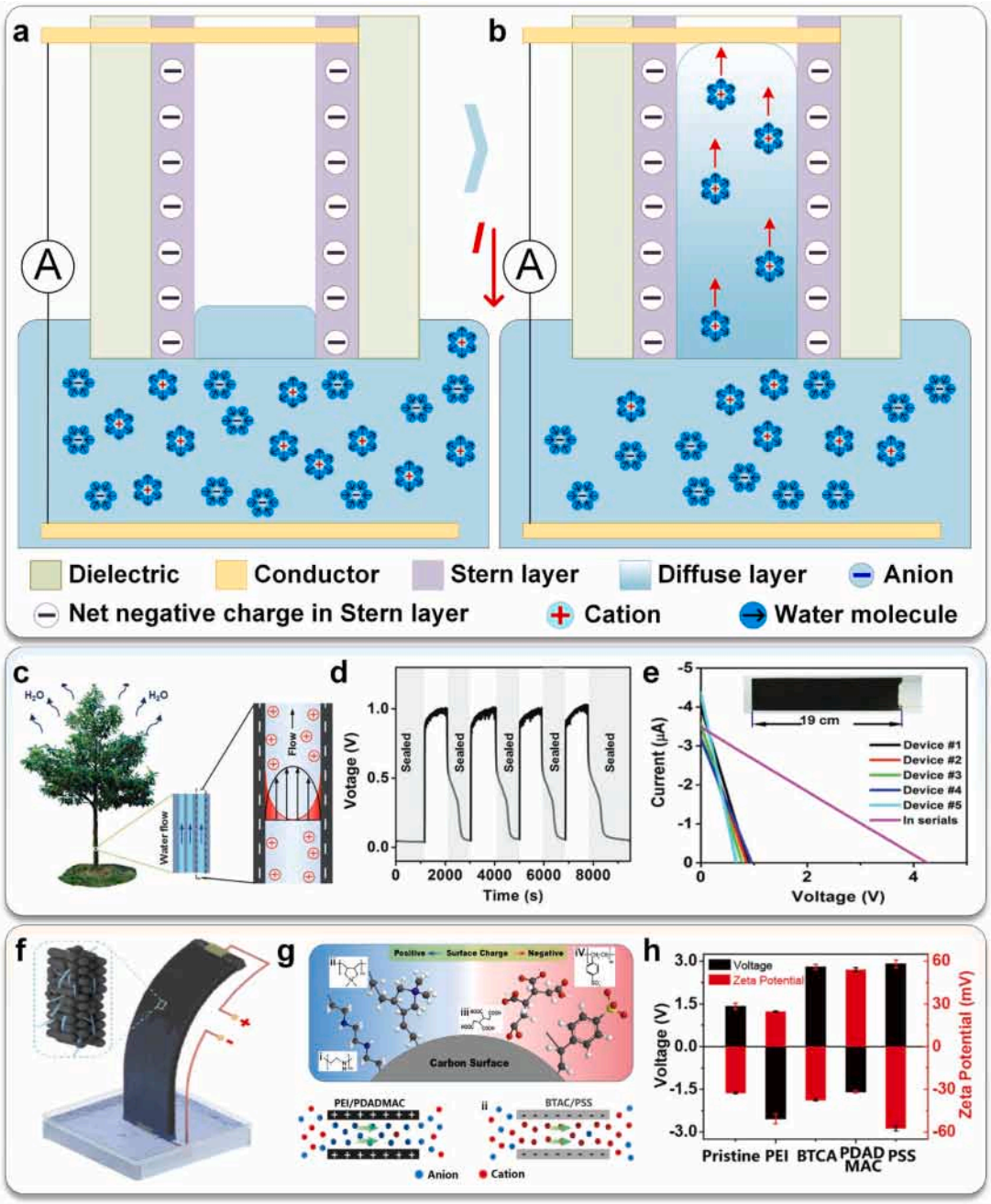

Fig. 11. The operating mechanism of MEGs based on evaporation-driven transport of specific polar ions and the output characteristics of its typical devices. a, b, The operating mechanism of MEGs based on evaporation-driven transport of specific polar ions. c, A typical MEG based on evaporation-driven transport of specific polar ions was developed by Ding et al. in 2017 [124]. d, The MEG could produce a V_{OC} of up to 1 V in an ambient environment. e, The output performance of this MEG could be increased by increasing the device's area and connecting multiple units. f, In 2019, Li et al. developed a high-performance MEG that could achieve adjustable higher voltage output [125]. g, This MEG demonstrated adjustable output voltages by modifying the surface functional groups of carbon nanoparticles with various molecules or polymers. h, Performance evaluations revealed significant voltage variations depending on modifying the surface functional groups of carbon nanoparticles. c–e, Copyright 2017, WILEY-VCH Verlag GmbH & Co. KGaA. f-h, Copyright 2019, Elsevier Ltd.

maintain this performance steadily for 220 h (Fig. 11d). Moreover, the device exhibited good reproducibility and stability under varying environmental humidity and airflow conditions. When connected to external loads with different resistances, the maximum output power could reach 172 nW, with a power density of approximately 8.1 μW/cm^3. This capability indicated the potential for enhancing performance by increasing the device's area and connecting multiple units (Fig. 11e). In practical applications, the MEG could supply power to small electronic devices or effectively charge capacitors and it could charge a 47 μF capacitor to 3.5 V within 100 s. This research provided a viable solution for future self-powered electronic devices, showcasing broad application prospects in areas such as wearable technology, environmental monitoring, and portable electronics. To further achieve adjustable higher voltage output, in 2019, Li et al. developed a high-performance MEG based on evaporation-driven transport of specific polar ions using a flexible, freestanding carbon film [125] (Fig. 11f). This MEG demonstrated adjustable output voltages ranging from −3 V to +3 V by modifying the surface functional groups of carbon nanoparticles with various molecules or polymers. Functional groups such as hydroxyl, carbonyl, and carboxyl on the carbon nanoparticle

surface created a negative surface charge, generating electrokinetic voltage during water flow through the nanochannels (Fig. 11g). When carbon nanoparticles were modified with positively charged polymers like polyethyleneimine (PEI), electrostatic interactions between the cationic polymer and the negative carbon nanoparticle surface resulted in spontaneous adsorption, transforming the surface charge from negative to positive. Performance evaluations revealed significant voltage variations depending on the modification, with PEI and poly-sodium styrene sulfonate (PSS)-modified devices producing maximum voltages exceeding 3 V (Fig. 11h). This research underscored the role of surface modifications in optimizing energy harvesting devices, offering promising advancements in sustainable energy technologies. Additionally, a hybrid design, comprising two laminated carbon films with opposing ion affinities, further enhanced the MEG's performance, achieving a V_{OC} of up to 5 V.

7. Various types of osmotic power sources

To generate a more independent and large-scale constant current output, conventional osmotic power sources have been developed. These systems leveraged concentration gradients between solutions to drive the movement of specific-polarity ions within the Debye length of the EDL at ion channel surfaces, thereby generating stable, large-scale power outputs. Notably, 2D nanofluidic channels exhibited enhanced ionic mobility and permeability due to anomalous ion dynamics in nanoconfined environments. This enhancement significantly boosted the power output of osmotic power sources, making them more efficient and effective for energy harvesting applications.

7.1. Advancements of osmotic power sources

To enhance the directed migration of ions within the Debye length of

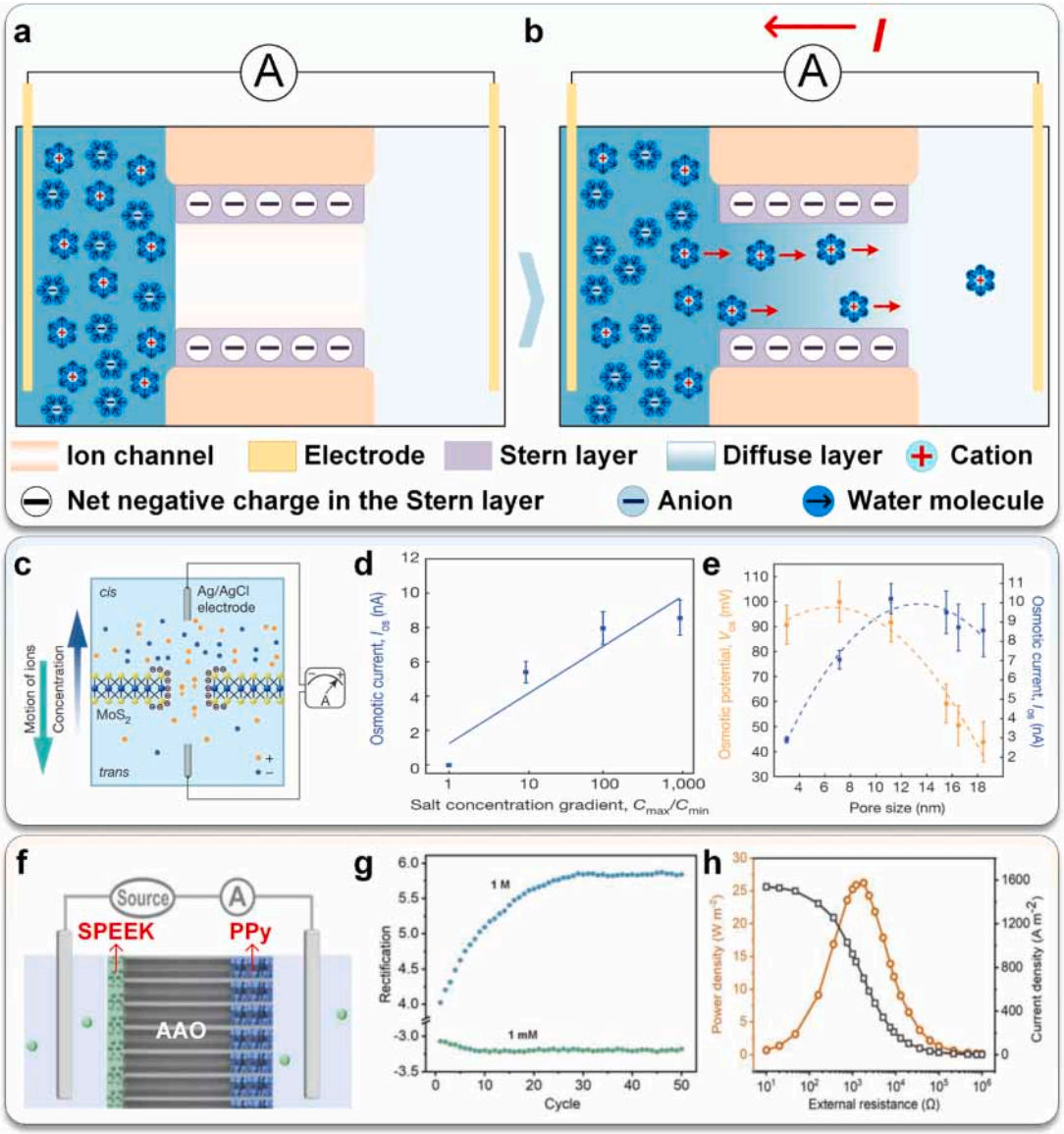

Fig. 12. The operating mechanism of conventional osmotic power sources and the output characteristics of its typical devices. a, b, The operating mechanism of conventional osmotic power sources. c, A more efficient osmotic power source using single-layer MoS_2 nanopores was developed by Feng et al. in 2016 [159]. d, The generated current exhibited a positive correlation with the concentration gradient. e, The power density reached 10^6 W/m^2. f, A novel osmotic power source utilizing MoS_2 nanofluidic channels was developed by Hao et al. in 2022 [160]. g, It could adaptively adjust its conductivity in different salinity environments by integrating ionomer and conducting polymer components. h, The osmotic power source achieved a remarkable power density of 26.22 W/m^2. c–e, Copyright 2016, Springer Nature Limited. f-h, Copyright 2022, Wiley-VCH GmbH.

the EDL, conventional osmotic power sources have been innovatively developed. These advanced systems exploit concentration gradients between distinct solutions to facilitate the movement of specific polar ions along the surfaces of ion channels. This strategic approach effectively generates a substantial and stable power output, significantly boosting energy conversion efficiency. When ion channels are positioned between solutions of varying concentrations, the resulting liquid flow forms an EDL characterized by unique charge properties (Fig. 12a). The ion concentration gradient allows oppositely charged ions to traverse the charged channels with remarkable efficiency, while similarly charged ions encounter resistance and are effectively blocked. This rapid and directed migration of specific polar ions within the Debye length not only induces a stable electric current but also enhances the reliability of the power output (Fig. 12b). Compared to MEGs based on evaporation-driven transport of specific polar ions, these concentration gradient-driven conventional osmotic power sources could significantly enhance energy output and optimize energy conversion efficiency.

In 2016, Feng et al. developed a more efficient osmotic power source using single-layer MoS_2 nanopores [159] (Fig. 12c), which could generate ultra-high power density as a single-ion channel osmotic power source. By introducing MoS_2 nanopores into potassium chloride solutions of varying concentrations, it was found that the generated current exhibited a positive correlation with the concentration gradient, highlighting the critical role of concentration difference in the electrical current generation (Fig. 12d). Furthermore, smaller nanopore diameters demonstrated superior voltage performance and ion selectivity, whereas increased pore size led to reduced ion selectivity, significantly impacting current output. The relationship between current, concentration ratio, and pore conductivity was validated through molecular dynamics simulations and continuum models. When the pore diameter was approximately 10 nm, the power density reached 10^6 W/m^2 (Fig. 12e), indicating exceptional energy generation capabilities. Additionally, the study explored the power generation potential of multilayer MoS_2 membranes, revealing a significant decrease in efficiency with increasing layer count, thereby emphasizing the advantages of single-layer MoS_2 membranes in osmotic power generation and their potential in renewable energy applications. The above-mentioned osmotic power sources were based on single-ion channels and had higher power density at the micro level. To enhance the practical applicability, Hao et al. (2022) developed a novel osmotic power source utilizing MoS_2 nanofluidic channels that adaptively adjust their conductivity in varying salinity environments by integrating ionomer and conducting polymer components [160] (Fig. 12f). Under low salinity conditions, polypyrrole (PPy) chains exhibited lower charge density and remained collapsed, resulting in the preferential transport of ions from the ionomer side to the PPy side (Fig. 12g). In contrast, under high salinity conditions, the charge and structure of PPy change, reversing the direction of ion transport. Experimental results indicated that increased salinity significantly enhances the doping levels and surface charge density of PPy, leading to improved current output. With a nanopore diameter of approximately 10 nm, the osmotic power source achieved a remarkable power density of 26.22 W/m^2 (Fig. 12h), showcasing its superior energy generation capabilities. The dynamic adaptation of the membrane was further evidenced by the increasing transmembrane current over time, underscoring its robust salt tolerance and energy conversion efficiency. This membrane exhibited excellent salt tolerance in solutions of varying concentrations, making it suitable for harvesting and converting osmotic energy between seawater and freshwater.

7.2. Osmotic power sources based on 2D nanofluidic channels

In the nano-confined region, ions were significantly influenced by interface effects, and the nanoscale confinement reduces interactions between ions and water molecules. This unique environment could lead to higher mobility and permeability of partially hydrated ions compared to fully hydrated ions in conventional ion channels. To enhance the macroscopic output capability of conventional osmotic power sources, utilizing 2D nanofluidic channels in nano-confined environments as ion-selective channels could substantially improve device performance. GO exemplified a promising 2D nanofluidic material [129,158], characterized by an interlayer spacing of 7.7 Å and a monolayer thickness of 3.4 Å, resulting in an effective channel size of approximately 4.3 Å. This effective dimension was notably smaller than the typical diameter of the hydrated shell surrounding metal ions, thereby limiting the extent of hydration during ion transport. Consequently, in osmotic power sources utilizing GO 2D nanofluidic channels, metal cations could migrate more effectively towards reduced graphene oxide (rGO) under the influence of a concentration gradient (Fig. 13), benefiting from enhanced mobility and permeability. Moreover, the nanoscale structural characteristics of GO might facilitate increased interactions between ions and the material interface, further optimizing performance. This enhancement in ion transport and interaction dynamics not only underpinned the efficiency of the osmotic power source but also broadened the potential applications of GO in energy conversion and storage technologies.

In 2021, Yang et al. drew inspiration from electric eels to develop a fully printable all-solid-state osmotic power source based on graphene inks [147] (Fig. 14a). Each cell in this power source achieved a V_{OC} of 1.2 V, which was eight times higher than that of the biological electrode. This elevated voltage was attributed to the significant cation concentration difference maintained by GO materials, facilitating exceptional energy output. When stored in low-humidity conditions, ion transport was restricted, resulting in negligible self-discharge and ensuring prolonged shelf life. Galvanostatic discharge tests conducted at 25 °C and 70% relative humidity demonstrated stable voltage output (Fig. 14b), making it suitable for practical applications. The research team employed a Peano curve as the printed pattern to enhance the effective length of the cells, thereby further improving power output. Under high-humidity conditions, the I_{SC} reached 170 μA, with a power density of 2.5 mW/cm^3 (Fig. 14c), comparable to that of lithium thin-film batteries. This study provided a simple yet effective approach to harnessing ion gradients for scalable green power, opening new avenues for future energy technologies. To further enhance the output performance, Yang et al. (2024) developed a solid-state osmotic power source leveraging the efficient ion transport dynamics within 2D nanofluidic channels of GO and optimized interfacial redox reactions [129] (Fig. 14d). A vertical design strategy was implemented utilizing the edge of a PET substrate and Kapton film in this source, effectively reducing the ion transport distance, which was equivalent to decreasing the thickness of the ion-selective membrane. They investigated the transport rates of alkali metal ions within the GO nanofluidic channels through experiments and simulations, selecting the fastest cation to minimize internal resistance. Additionally, tailored interfacial redox reactions were introduced on the electrode surface to enhance power output, enabling the device to discharge at 100 μA (Fig. 14e) and achieving an I_{SC} of nearly 1 mA. This combination of efficient cation transport and optimized redox reactions culminated in a maximum output power density of 15,900 W/m^2 (Fig. 14f). Overall, this research laid a foundational understanding of nanoscale ion dynamics and the rational design of ion-electronic energy systems, indicating significant potential for future studies on various 2D nanomaterials and the fine-tuning of redox reactions in the development of efficient and renewable energy sources.

Beyond functioning as an energy storage device, the ultrathin planar osmotic power source could seamlessly integrate with other planar energy harvesting technologies to establish a comprehensive energy management system, facilitating prolonged and stable operation. In 2022, Wei et al. leveraged the efficient selective ion transport dynamics inherent to the 2D nanofluidic channels of GO to develop a high-performance osmotic power source [161] (Fig. 14g). Their research demonstrated that GO nanopores exhibit a strong preference for the transport of K^+ ions, achieving a selectivity ratio exceeding 100 compared to anions like Cl^-. Additionally, hydrated K^+ ions migrate significantly faster—by several orders of magnitude—than most other

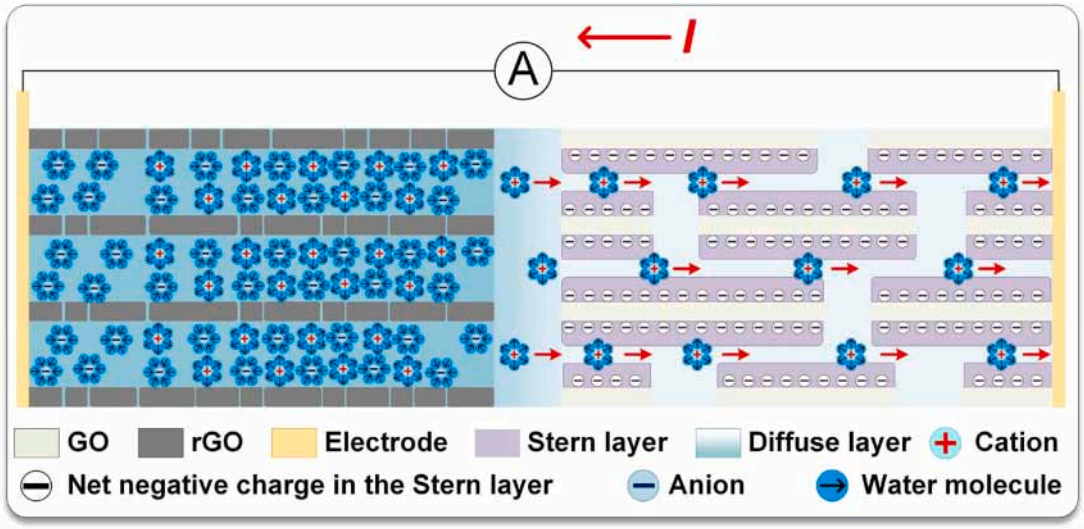

Fig. 13. The operating mechanism of osmotic power sources based on 2D nanofluidic channels.

hydrated ions within these nanofluidic channels. This remarkable ion transport capability culminates in a maximum volumetric power density of 28 mW/cm^3, comparable to that of supercapacitors, while the maximum volumetric energy density reaches 6 mWh/cm^3, approaching the performance of thin-film lithium batteries. This ultrathin, printable osmotic power source could be effectively coupled with TENGs to create a self-charging iontronics system (Fig. 14h), thereby enhancing energy management efficiency and making it ideal for extended stable operation. In 2023, Peng et al. developed a paper-based osmotic power source leveraging the efficient Li^+ transport within the 2D nanofluidic channels of GO, combined with finely tuned interfacial redox reactions. This paper-based power source demonstrated impressive performance, achieving an areal power density of 1095.05 mW/cm^2, surpassing that of most flexible batteries. Moreover, the potential for integration was highlighted by demonstrating an energy management system—comprising a paper-based TENG and the osmotic power source—alongside a wireless sensing system, all printed on a single piece of paper [162] (Fig. 14i). This advancement underscored the significant potential of such integrative iontronics power sources in the realm of soft, wireless, and disposable electronics. In addition to GO, MXene also could serve as an excellent 2D nanofluidic material. Inspired by the rapid water transport observed in xylem vessel elements, Qian et al. designed a horizontal transport MXene (H-MXene) prepared by simple vacuum filtration in 2024 (Fig. 14j). The H-MXene can withstand extreme saline-alkali conditions, and significantly outperforms that with vertical ionic transport channels (V-MXene) in ion selectivity and permeability, achieving a current density over three orders of magnitude higher without significant polarization, an osmotic power density of 9.47 W/m^2, and an exceptional energy conversion efficiency of 45.7% (Fig. 14k). Molecular dynamics (MD) simulation results show that MXene nanochannels exhibit excellent cation selectivity, with significantly higher diffusion coefficients for Na^+ and H^+ in H-MXene compared to V-MXene. Specifically, the transport rates of Na^+ and H^+ in H-MXene are 2.57 and 2.32 times higher, respectively, than in V-MXene (Fig. 14l). This work demonstrates that H-MXene selective permeation membranes with horizontal ionic transport channels achieve a trade-off between selectivity and permeability, bridging the gap in osmotic energy conversion in saline-alkaline environments.

8. Various water-based nanogenerators

The aforementioned types of nanogenerators demonstrated stable operating mechanisms and superior output characteristics (Table 1), highlighting their substantial application potential in energy harvesting fields. Firstly, in the field of ocean energy harvesting, Liang et al. designed the S-L TENG aimed at enhancing the efficiency of water wave energy harvesting in 2023 [164] (Fig. 15a). This generator operated as a mechanically driven AC SL TENG, achieving effective output by dynamically regulating the charge distribution within the diffuse layer. The study explored the output characteristics of the S-L TENG in pure water and analyzed its performance under varying conditions, such as liquid concentration, motion frequency, and height. Subsequently, the generator was extended into an array to adapt to irregular water wave environments, successfully demonstrating its application potential for powering signal lights, digital thermometers, and water quality detectors. Especially, the study showcased the practical application of the generator array in powering portable electronic devices, confirming its significant potential for efficient ocean energy harvesting and the development of sustainable portable electronics. As an innovative method for energy collection and conversion, the S-L TENG array could not only effectively harness ocean energy to power small devices but also provide corrosion protection for metal materials in marine environments, enabling diversified utilization of ocean energy. In 2021, Sun et al. presented the structure and operational mechanism of a S-L TENG array applied in a self-powered cathodic protection system [165] (Fig. 15b). This system consisted of two parallel mechanically driven AC S-L TENGs connected to a rectifying bridge, ensuring generated electrons consistently flow towards the steel to provide cathodic protection. In immersion tests conducted in a 3.5 wt% NaCl solution, the steel not connected to the S-L TENGs exhibited noticeable green corrosive pitting within 1 h, with the corrosion area significantly increasing over time. In contrast, the carbon steel connected to the S-L TENGs showed no evident signs of corrosion. This research demonstrated the considerable potential of S-L TENGs in marine energy utilization and metal corrosion protection, highlighting their broad application prospects. Secondly, in addition to directly harnessing ocean energy through S-L TENGs, salinity gradient energy could also be effectively harvested using osmotic power devices that exploit the salinity difference between seawater and freshwater. In 2024, drawing inspiration from the rapid water transport observed in xylem conduits, Qian et al. introduced a novel horizontal transport MXene aimed at improving ion selectivity and permeability of osmotic power sources [163] (Fig. 15c). When tested in an artificial seawater and river environment with a salinity gradient of 0.5 M/0.01 M, the negatively charged nanoconfined channels of this MXene effectively facilitated the selective movement of sodium ions, yielding a membrane potential of 96.6 mV and a diffuse current of 11.42 μA. The

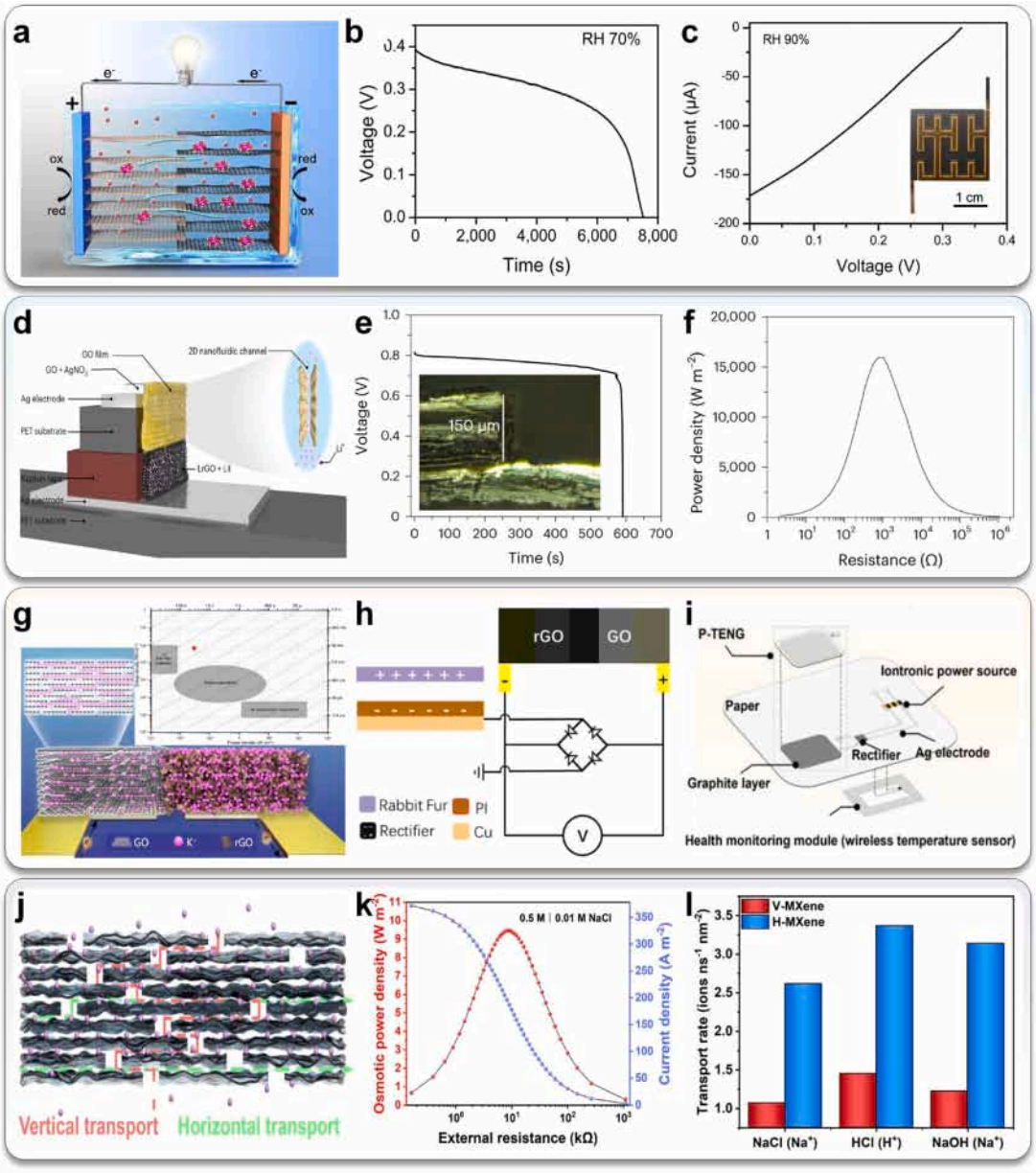

Fig. 14. The output characteristics of typical osmotic power sources based on 2D nanofluidic channels. a, An osmotic power source was developed by Yang et al. in 2021 [147]. b, Galvanostatic discharge tests demonstrated its stable voltage output. c, Its power density could reach 2.5 mW/cm^3. d, A vertical osmotic power source was developed by Yang et al. in 2024 [129]. e, The device could discharge stably at 100 μA. f, Its maximum output power density could reach 15,900 W/m^2. g, A high-performance osmotic power source was developed by Wei et al. in 2022 [161]. h, This osmotic power source could be effectively coupled with TENGs to create a self-charging iontronics system. i, In 2023, Peng et al. demonstrated an integrative iontronics power source [162]. j, A H-MXene prepared by simple vacuum filtration was designed by Qian et al. in 2024 [163]. k, Its power density could reach 9.47 W/m^2. l, The transport rates of Na^+ and H^+ in H-MXene are 2.57 and 2.32 times higher, respectively, than in V-MXene. a–c, Copyright, 2021, The author(s) retains copyright to individual articles, and the NAS retains an exclusive license to publish these articles and holds copyright to the collective work. d–f, Copyright 2024, The Author(s), under exclusive licence to Springer Nature Limited. g and h, Copyright 2022, The Author(s), Distributed under the terms of the Creative Commons CC BY license. i, Copyright 2023, Wiley-VCH GmbH. j-l, Copyright 2024, Wiley-VCH GmbH.

device achieved an impressive osmotic power density of 9.47 W/m^2, surpassing the commercial benchmark of 5.0 W/m^2, while also exhibiting excellent energy conversion efficiency. This research underscored the impressive capabilities of horizontal transport MXene in the context of varying salinity gradients, especially its low internal membrane resistance and high power output, positioning it as a promising candidate for effectively harnessing salinity gradient energy. In 2024, Yang et al. developed a nano-porous structure aimed at optimizing the generation efficiency of osmotic power sources [166] (Fig. 15d). This structure was created by electrochemically modifying one-dimensional metal-organic framework (MOF) nanoparticles onto 2D MXene nanosheets. This composite membrane demonstrated excellent cation selectivity, achieving output power densities of up to 10.71 W/m^2 and 35.04 W/m^2 at concentration gradients of 50-fold and 500-fold, respectively. Furthermore, it maintained stable power generation over a month, underscoring its practical applicability. The osmotic power source showed promising potential for future salinity gradient energy harvesting, indicating its viability as an effective solution in the field of renewable energy.

Evaporation energy represents a significant component of water-

Table 1
Output characteristics of typical prototypes of different types of nanogenerators.

Typical prototype of different types of nanogenerators		V_{OC} (V)	I_{SC} (μA)	P_R density (mW/cm^2)
S-L TENGs	Mechanically driven DC S-L TENG [83]	0.7	0.3	~ 1 × 10^{-6}
	Mechanically driven AC S-L TENG [167]	150	270	5.01
	Electrostatically driven AC S-L TENG [103]	1400	25.96	0.17
TINGs	TING based on asymmetric EDLs [96]	0.25	2600	8.45
	TING based on regulating charge density of the diffuse layer [95]	1750	36	12.64
Hydrovoltaic technology [102]		7.3	0.011	~ 5.7 × 10^{-6}
MEGs	MEGs based on humidity-induced functional group hydrolysis [146]	1.1	3.4	2.6
	MEGs based on evaporation-driven transport of specific polar ions [125]	5	1.5	~ 1.9 × 10^{-3}
Osmotic power sources	Conventional osmotic power sources [160]	0.16	83	2.62
	Osmotic power sources based on 2D nanofluidic channels [129]	1.07	1000	1590

based energy. Thirdly, in the pursuit of efficient energy harvesting from evaporation, Yun et al. developed an MEG based on evaporation-driven transport of specific polar ions in 2022 [123] (Fig. 15e). This device aimed to enhance energy generation efficiency by utilizing a broader range of water resources. The MEG operated by selectively permeating cations, generating an additional potential difference within a polymer matrix containing sulfonate functional groups, thereby boosting energy output. Compared to carbon-based MEGs, it exhibited an energy density increase of 80% to 250% under identical resistance conditions. Notably, seawater, with its high concentration of small-radius ions (Na^+), generated the higher V_{OC} and I_{SC} during evaporation-driven flow. In a seawater environment, the MEG demonstrated an impressive areal power density of 0.45 μW/cm^2, sufficient to directly power low-energy electronic devices. Consequently, the MEG was particularly well-suited for sustainable energy harvesting systems that capitalize on seawater evaporation. In addition to generating electricity through liquid evaporation, MEGs have demonstrated significant potential in wastewater treatment. In 2023, Hao et al. developed an innovative MEG based on a graphene/alginate hydrogel, featuring efficient solar-driven pure water extraction and exceptional antifouling capabilities [168] (Fig. 15f). It could effectively reject over 99.5% of volatile organic compounds, 99.3% of ions, and 100% of non-aqueous contaminants and bacteria, with an ion rejection rate of 94.9% in seawater environments. The advanced design of this material enabled outstanding clean water collection and antifouling performance in complex aqueous environments, highlighting its importance in promoting the application of solar-driven evaporative water purification technologies. Fourthly, in addition to various types of water-based energy harvesting, S-L TENGs could also effectively harvest biomechanical energy. Fourthly, raindrops represented a significant component of water-based energy, which could be effectively harvested by S-L TENGs. In 2020, Xu et al. developed a high-performance mechanically driven AC S-L TENG designed to efficiently harvest energy from impinging water droplets [167] (Fig. 15g). The device was structured with a PTFE film, an indium tin oxide substrate, and an aluminum electrode. Upon water droplet impact, the spreading of the droplet forms a closed electrical circuit from previously disconnected components, significantly transforming traditional interfacial effects into bulk effects and enhancing the instantaneous power density by several orders of magnitude. Experimental results indicated that after approximately 16,000 consecutive impacts, the PTFE surface could store stable charges, enabling the device to instantaneously illuminate 400 LEDs. The device exhibited a V_{OC} of 143.5 V and an I_{SC} of 270.0 μA, with an instantaneous P_R density of 50.1 W/m^2—substantially surpassing the output capabilities of conventional S-L TENGs. These findings demonstrated this S-L TENG's superiority in water droplet energy harvesting and conversion, highlighting its significant potential for various applications. Furthermore, in 2022, Ye et al. developed a highly transparent, large-area, and efficient rain-driven S-L TENG array based on the principle of similarity [169] (Fig. 15h), which could be effectively integrated with solar panels for simultaneous energy harvesting from irregular raindrops and sunlight. The study demonstrated that under rainy conditions, the average power density of the S-L TENG array reached 40.80 mW/m^2, significantly surpassing the solar cell's output of 37.03 mW/m^2. This research offered a novel approach for future self-powered environmental monitoring technologies, showcasing the efficacy of synergistic energy harvesting from both raindrops and sunlight. The aforementioned applications illustrate that diverse types of nanogenerators were capable of effectively harvesting various forms of water-based energy, highlighting their significant potential for future applications in sustainable energy harvesting.

9. Conclusion and perspectives

In summary, this review provides a comprehensive overview of key nanogenerator technologies that leverage dynamic regulation of the EDL, categorizing them into five primary types: S-L TENGs, TINGs, hydrovoltaic technology, MEGs, and osmotic power sources. Firstly, S-L TENGs operate by adjusting the charge distribution on the EDL near dielectric materials through mechanical movement or electrostatic fields and can be further divided into mechanically driven DC S-L TENGs, mechanically driven AC S-L TENGs, and electrostatically driven AC S-L TENGs. These devices exploit the high internal resistance of dielectric materials to generate high-voltage outputs. Consequently, S-L TENGs provide a promising solution for capturing and converting wave energy into usable electrical power, particularly in applications requiring high voltage for energy conversion or storage. Secondly, TINGs achieve effective pulsed DC outputs by creating asymmetric EDLs at the ultra-thin interface between conductors and liquids or by modulating the charge density in the diffuse layer of the EDL adjacent to dielectric surfaces. Since TINGs can generate efficient pulsed DC outputs by harvesting water-based energy, they are particularly well-suited for providing stable power to intermittent sensors or sensing nodes that operate in a pulsed or low-duty cycle manner (such as temperature sensors, humidity sensors, air quality sensors, and others). This characteristic allows TINGs to effectively power such devices, ensuring a reliable energy supply for applications that do not require continuous power but rather periodic bursts of energy. Thirdly, hydrovoltaic technology generates a constant current through the mechanical movement of the EDL at the ultra-thin conductor-liquid interface, making it well-suited for continuous power generation. With its stable low-amplitude current output, hydrovoltaic technology is particularly effective in powering sensing dielectric devices that require continuous, low-power energy, especially in aquatic environments. By efficiently harvesting energy from flowing water, it holds significant potential for applications in remote monitoring, environmental sensing, and other fields that demand a reliable, sustained energy supply. Fourthly, MEGs facilitate the directional movement of ions within the Debye length of the EDL by inducing ion concentration gradients via humidity-triggered functional group hydrolysis or through evaporation-driven transport of specific polar ions through charged channels, allowing for convenient independent constant current generation. Consequently, MEGs are highly versatile and can produce reliable current outputs in a variety of aquatic environments, regardless of water flow conditions. This makes them particularly effective for energy harvesting in diverse settings, ranging from natural water bodies to controlled humid environments. Such capabilities provide a consistent and sustainable power source for small sensor nodes, such as those used in real-time water quality monitoring

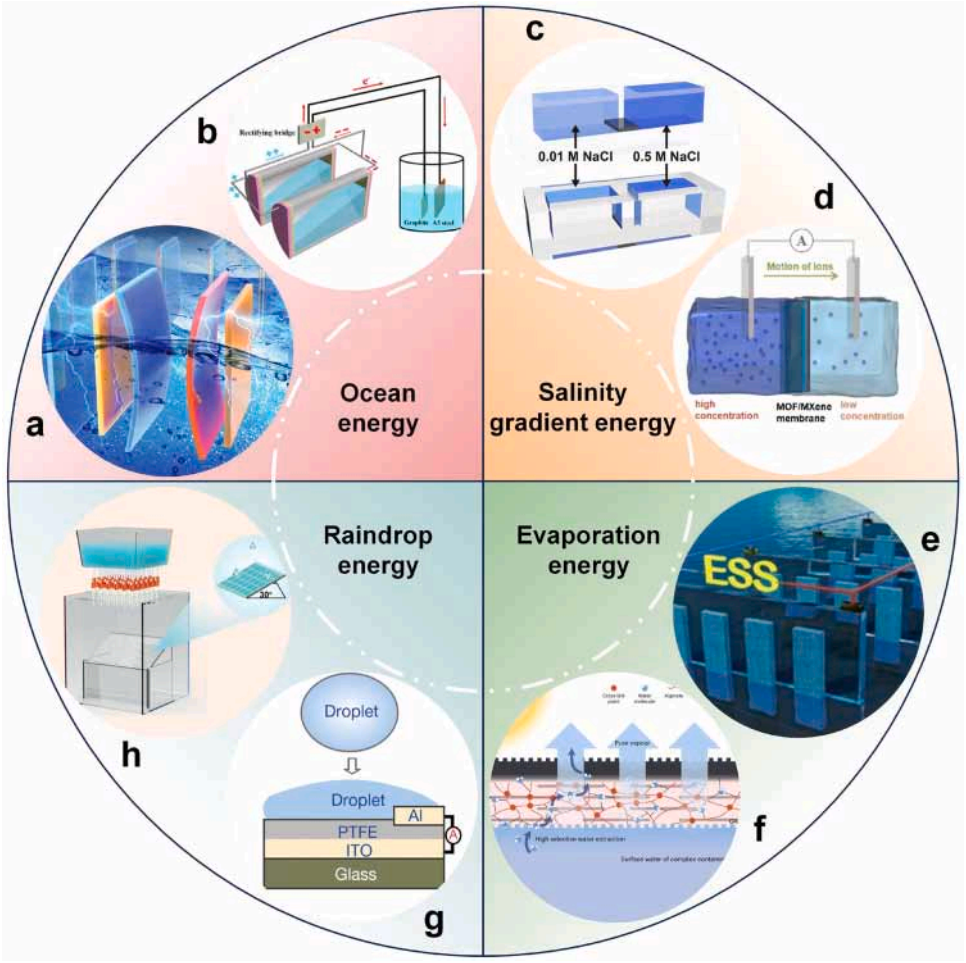

Fig. 15. Various types of nanogenerators could effectively harvest different forms of water-based energy. a, The S-L TENG was designed by Liang et al. in 2023 to enhance the efficiency of water wave energy harvesting [164]. b, The S-L TENG array was developed by Sun et al. in 2021 [165]. c, A novel horizontal transport MXene was introduced by Qian et al. in 2024 [163]. d, A nano-porous structure was developed by Yang et al. in 2024 [166]. e, An MEG based on evaporation-driven transport of specific polar ions was developed by Yun et al. in 2022 [123]. f, In 2023, an innovative MEG based on a graphene/alginate hydrogel was developed by Hao et al. [168]. g, In 2020, a high-performance mechanically driven AC S-L TENG was developed by Xu et al. [167]. h, in 2022, a highly transparent, large-area, and efficient rain-driven S-L TENG array was developed by Ye et al. [169]. a, Copyright 2023, Wiley-VCH GmbH. b, Copyright 2020, Elsevier Ltd. c, Copyright 2024, Wiley-VCH GmbH. d, Copyright 2024, Published by Elsevier Ltd. e, Copyright 2022, Elsevier Ltd. f, Copyright 2023, The Author(s). Distributed under the terms of the Creative Commons CC BY license. g, Copyright 2020, The Author(s), under exclusive licence to Springer Nature Limited. h, Copyright 2023, Wiley-VCH GmbH.

and environmental sensing. Fifthly, osmotic power sources utilize concentration gradients between solutions to drive the movement of specific-polarity ions within the EDL at ion channel surfaces, enabling large-scale stable power output. Notably, 2D nanofluidic channels enhance ionic mobility and permeability due to the incomplete hydration of ions in nanoscale environments, significantly boosting osmotic power generation. Furthermore, this review also explores the practical applications of these nanogenerator technologies in various water-based energy harvesting contexts, aiming to guide the selection and optimization of suitable technologies for real-world applications. So, osmotic power sources are promising green energy technology with significant potential, particularly for large-scale energy harvesting from the salinity difference between seawater and freshwater. By efficiently harnessing the natural salinity gradient, osmotic power sources provide a continuous and stable energy source, aligning with environmental sustainability and development principles.

Currently, nanogenerators utilized for water-based energy harvesting present several avenues for optimization, including the enhancement of conversion efficiency, increased material stability, reduced manufacturing costs, improved integration, and better environmental adaptability. To address these challenges, future research directions may encompass the development of corrosion-resistant and more stable novel materials, optimization of the nanogenerator's structural design to enhance efficiency, exploration of more cost-effective production processes, improvement of compatibility with existing devices, and the integration of smart control technologies for real-time monitoring and adjustment. These initiatives are anticipated to significantly enhance the overall performance of nanogenerators and facilitate their widespread application in practical settings.

CRediT authorship contribution statement

Xiang Li: Writing – review & editing. **Zhong Lin Wang:** Writing – review & editing. **Di Wei:** Writing – review & editing.

Declaration of competing interest

The authors declare no competing interests.

Acknowledgements

This work was supported by the National Natural Science Foundation (grant number 22479016).

Supplementary materials

Supplementary material associated with this article can be found, in the online version, at doi:10.1016/j.nwnano.2024.100062.

References

[1] H. Ledford, Do soaring energy costs mean we are using less? Nature 610 (2022) 619.
[2] E. Shove, Time to rethink energy research, Nat. Energy 6 (2020) 118–120.
[3] J. Agbenyega, Energy crisis, Mater. Today 12 (2009) 1.
[4] J. Ren, D. Zhao, Recent advances in reticular chemistry for clean energy, global warming, and water shortage solutions, Adv. Funct. Mater. (2023) 2307778.
[5] R. Pande, The climate crisis is a crisis of inequality, Science 381 (2023) eadk3500.
[6] S. Garimella, K. Lockyear, D. Pharis, O. El Chawa, M.T. Hughes, G. Kini, Realistic pathways to decarbonization of building energy systems, Joule 6 (2022) 956–971.
[7] S.R. Nicholson, N.A. Rorrer, A.C. Carpenter, G.T. Beckham, Manufacturing energy and greenhouse gas emissions associated with plastics consumption, Joule 5 (2021) 673–686.
[8] J. Huang, X. Zhang, Q. Zhang, Y. Lin, M. Hao, Y. Luo, Z. Zhao, Y. Yao, X. Chen, L. Wang, S. Nie, Y. Yin, Y. Xu, J. Zhang, Recently amplified arctic warming has contributed to a continual global warming trend, Nat. Clim. Chang. 7 (2017) 875–879.
[9] T.L. Frolicher, E.M. Fischer, N. Gruber, Marine heatwaves under global warming, Nature 560 (2018) 360–364.
[10] G.C. Johnson, J.M. Lyman, Warming trends increasingly dominate global ocean, Nat. Clim. Chang. 10 (2020) 757–761.
[11] R. Newman, I. Noy, The global costs of extreme weather that are attributable to climate change, Nat. Commun. 14 (2023) 6103.
[12] P. Stott, CLIMATE CHANGE. How climate change affects extreme weather events, Science 352 (2016) 1517–1518.
[13] Extreme weather events are the new normal, Nature 548 (2017) 499.
[14] C. Ibanez, N. Caiola, J. Barquin, O. Belmar, X. Benito-Granell, F. Casals, S. Fennessy, J. Hughes, M. Palmer, J. Penuelas, E. Romero, J. Sardans, M. Williams, Ecosystem-level effects of re-oligotrophication and N:P imbalances in rivers and estuaries on a global scale, Glob. Chang. Biol. 29 (2023) 1248–1266.
[15] J. Peñuelas, B. Poulter, J. Sardans, P. Ciais, M. van der Velde, L. Bopp, O. Boucher, Y. Godderis, P. Hinsinger, J. Llusia, E. Nardin, S. Vicca, M. Obersteiner, I.A. Janssens, Human-induced nitrogen–phosphorus imbalances alter natural and managed ecosystems across the globe, Nat. Commun. 4 (2013) 2934.
[16] T. Yao, T. Bolch, D. Chen, J. Gao, W. Immerzeel, S. Piao, F. Su, L. Thompson, Y. Wada, L. Wang, T. Wang, G. Wu, B. Xu, W. Yang, G. Zhang, P. Zhao, The imbalance of the Asian water tower, Nat. Rev. Earth Environ. 3 (2022) 618–632.
[17] J.M. Turner, The matter of a clean energy future, Science 376 (2022) 1361.
[18] J.D. Ampah, C. Jin, H. Liu, S. Afrane, H. Adun, D. Morrow, D.T. Ho, Prioritizing non-carbon dioxide removal mitigation strategies could reduce the negative impacts associated with large-scale reliance on negative emissions, Environ. Sci. Technol. 58 (2024) 3755–3765.
[19] C.J. Axon, R.C. Darton, Sustainability and risk – a review of energy security, Sustain. Prod. Consum. 27 (2021) 1195–1204.
[20] T. Bolsen, Framing renewable energy, Nat. Energy 7 (2022) 1003–1004.
[21] F. Contino, S. Moret, G. Limpens, H. Jeanmart, Whole-energy system models: the advisors for the energy transition, Prog. Energy Combust. Sci. 81 (2020) 100872.
[22] J. Schmidt, K. Gruber, M. Klingler, C. Klöckl, L. Ramirez Camargo, P. Regner, O. Turkovska, S. Wehrle, E. Wetterlund, A new perspective on global renewable energy systems: why trade in energy carriers matters, Energy Environ. Sci 12 (2019) 2022–2029.
[23] Wind power and solar photovoltaics found to have higher energy returns than fossil fuels, Nat. Energy 9 (2024) 775–776.
[24] B. Pickering, F. Lombardi, S. Pfenninger, Diversity of options to eliminate fossil fuels and reach carbon neutrality across the entire European energy system, Joule 6 (2022) 1253–1276.
[25] S. Kurtz, N. Haegel, R. Sinton, R. Margolis, A new era for solar, Nat. Photonics 11 (2017) 3–5.
[26] I.S. Osborne, Surveying the solar cell landscape, Science 352 (2016) 304–306.
[27] D.O. Hall, Solar energy, Nature 283 (1980) 915.
[28] X. Li, Y. Cao, X. Yu, Y. Xu, Y. Yang, S. Liu, T. Cheng, Z.L. Wang, Breeze-driven triboelectric nanogenerator for wind energy harvesting and application in smart agriculture, Appl. Energy 306 (2022) 117977.
[29] O.P. Mahela, A.G. Shaik, Comprehensive overview of grid interfaced wind energy generation systems, Renew. Sustain. Energy Rev. 57 (2016) 260–281.
[30] A. Sahin, Progress and recent trends in wind energy, Prog. Energy Combust. Sci. 30 (2004) 501–543.
[31] X. Li, D. Wei, Z.L. Wang, Direct current triboelectric nanogenerators, a perspective from material selections, Nanoenergy Adv. 3 (2023) 343–375.
[32] D. Cheng, Solar and wind, Nat. Clim. Chang. 13 (2023) 1020.
[33] X. Li, Q. Gao, Y. Cao, Y. Yang, S. Liu, Z.L. Wang, T. Cheng, Optimization strategy of wind energy harvesting via triboelectric-electromagnetic flexible cooperation, Appl. Energy 307 (2022) 118311.
[34] B.R. Sutherland, Diversifying progress in solar, Joule 2 (2018) 1383–1385.
[35] S.W. Lee, S. Bae, D. Kim, H.S. Lee, Historical analysis of high-efficiency, large-area solar cells: toward upscaling of perovskite solar cells, Adv. Mater. 32 (2020) 2002202.
[36] Q. Burlingame, X. Huang, X. Liu, C. Jeong, C. Coburn, S.R. Forrest, Intrinsically stable organic solar cells under high-intensity illumination, Nature 573 (2019) 394–397.
[37] S.M.F. Zhang, J.P. Seif, M.D. Abbott, A.H.T. Le, T.G. Allen, I. Perez-Wurfl, Z. Hameiri, Illumination-dependent temperature coefficients of the electrical parameters of modern silicon solar cell architectures, Nano Energy 98 (2022) 107221.
[38] I. Mora-Seró, G. Garcia-Belmonte, P.P. Boix, M.A. Vázquez, J. Bisquert, Impedance spectroscopy characterisation of highly efficient silicon solar cells under different light illumination intensities, Energy Environ. Sci. 2 (2009) 678–686.
[39] S. Liu, X. Li, Y. Wang, Y. Yang, L. Meng, T. Cheng, Z.L. Wang, Magnetic switch structured triboelectric nanogenerator for continuous and regular harvesting of wind energy, Nano Energy 83 (2021) 105851.
[40] S.C. Pryor, R.J. Barthelmie, A global assessment of extreme wind speeds for wind energy applications, Nat. Energy 6 (2021) 268–276.
[41] X. Gao, T. Wang, B. Li, H. Sun, H. Yang, Z. Han, Y. Wang, F. Zhao, Investigation of wind turbine performance coupling wake and topography effects based on LiDAR measurements and SCADA data, Appl. Energy 255 (2019) 113816.
[42] D.A. Katsaprakakis, A review of the environmental and human impacts from wind parks. A case study for the Prefecture of Lasithi, Crete, Renew. Sustain. Energy Rev. 16 (2012) 2850–2863.
[43] E. Rinne, H. Holttinen, J. Kiviluoma, S. Rissanen, Effects of turbine technology and land use on wind power resource potential, Nat. Energy 3 (2018) 494–500.
[44] F. Hyder, P. Baredar, K. Sudhakar, R. Mamat, Performance and land footprint analysis of a solar photovoltaic tree, J. Clean. Prod. 187 (2018) 432–448.
[45] L. Lombardi, B. Mendecka, E. Carnevale, W. Stanek, Environmental impacts of electricity production of micro wind turbines with vertical axis, Renew. Energy 128 (2018) 553–564.
[46] R. Nobre, S. Boulêtreau, F. Colas, F. Azemar, L. Tudesque, N. Parthuisot, P. Favriou, J. Cucherousset, Potential ecological impacts of floating photovoltaics on lake biodiversity and ecosystem functioning, Renew. Sustain. Energy Rev. 188 (2023) 113852.
[47] A. Lafitte, R. Sordello, V. de Crespin de Billy, J. Froidevaux, P. Gourdain, C. Kerbiriou, J. Langridge, G. Marx, B. Schatz, C. Thierry, Y. Reyjol, What evidence exists regarding the effects of photovoltaic panels on biodiversity? A critical systematic map protocol, Environ. Evid. 11 (2022) 36.
[48] Z.L. Wang, Catch wave power in floating nets, Nature 542 (2017) 159–160.
[49] Z. Zhang, X. Li, J. Yin, Y. Xu, W. Fei, M. Xue, Q. Wang, J. Zhou, W. Guo, Emerging hydrovoltaic technology, Nat. Nanotechnol. 13 (2018) 1109–1119.
[50] Z.L. Wang, T. Jiang, L. Xu, Toward the blue energy dream by triboelectric nanogenerator networks, Nano Energy 39 (2017) 9–23.
[51] Y. Jiang, X. Liang, T. Jiang, Z.L. Wang, Advances in triboelectric nanogenerators for blue energy harvesting and marine environmental monitoring, Engineering 33 (2024) 204–224.
[52] N. Kittner, Trading rivers for hydropower, Nat. Sustain. 7 (2024) 104–105.
[53] L. Jiang, X. Liu, J. Lv, G. Li, P. Yang, Y. Ma, H. Zou, Z.L. Wang, Fluid-based triboelectric nanogenerators: unveiling the prolific landscape of renewable energy harvesting and beyond, Energy Environ. Sci. 17 (2024) 3700–3738.
[54] Z. de Souza, G.L. Tiago Filho, R.M. Barros, I.F. Silva dos Santos, F.d.G.B. da Silva, M.D. Prado Leite, É.P. Prudente, The limit of sequential exploitation of a river's hydraulic potential, Renew. Sustain. Energy Rev. 68 (2017) 272–285.
[55] A. Farhadzadeh, M.R. Hashemi, S. Neill, Characterizing the Great Lakes hydrokinetic renewable energy resource: lake erie wave, surge and seiche characteristics, Energy 128 (2017) 661–675.
[56] C. Pheifer, C. Hill, Great Lakes wave energy resource classification and Blue Economy opportunities, Renew. Energy 235 (2024) 121213.
[57] X. Wang, S. Niu, Y. Yin, F. Yi, Z. You, Z.L. Wang, Triboelectric nanogenerator based on fully enclosed rolling spherical structure for harvesting low-frequency water wave energy, Adv. Energy Mater. 5 (2015) 1501467.
[58] T. Jiang, H. Pang, J. An, P. Lu, Y. Feng, X. Liang, W. Zhong, Z.L. Wang, Robust swing-structured triboelectric nanogenerator for efficient blue energy harvesting, Adv. Energy Mater. 10 (2020) 2000064.
[59] Y. Xi, H. Guo, Y. Zi, X. Li, J. Wang, J. Deng, S. Li, C. Hu, X. Cao, Z.L. Wang, Multifunctional TENG for blue energy scavenging and self-powered wind-speed sensor, Adv. Energy Mater. 7 (2017) 1602397.
[60] J.D. Isaacs, W.R. Schmitt, Ocean energy: forms and prospects, Science 207 (1980) 265–273.
[61] N. Zhang, C. Qin, T. Feng, J. Li, Z. Yang, X. Sun, E. Liang, Y. Mao, X. Wang, Non-contact cylindrical rotating triboelectric nanogenerator for harvesting kinetic energy from hydraulics, Nano Res. 13 (2020) 1903–1907.
[62] E. Segura, R. Morales, J.A. Somolinos, A. López, Techno-economic challenges of tidal energy conversion systems: current status and trends, Renew. Sustain. Energy Rev. 77 (2017) 536–550.
[63] D. Khojasteh, M. Lewis, S. Tavakoli, M. Farzadkhoo, S. Felder, G. Iglesias, W. Glamore, Sea level rise will change estuarine tidal energy: a review, Renew. Sustain. Energy Rev. 156 (2022) 111855.
[64] N. Guillou, G. Chapalain, S.P. Neill, The influence of waves on the tidal kinetic energy resource at a tidal stream energy site, Appl. Energy 180 (2016) 402–415.
[65] Z. Sun, X. Wen, L. Wang, J. Yu, X. Qin, Capacitor-inspired high-performance and durable moist-electric generator, Energy Environ. Sci. 15 (2022) 4584–4591.

[66] X. Liu, H. Gao, J.E. Ward, X. Liu, B. Yin, T. Fu, J. Chen, D.R. Lovley, J. Yao, Power generation from ambient humidity using protein nanowires, Nature 578 (2020) 550–554.
[67] R. Zhu, Y. Zhu, L. Hu, P. Guan, D. Su, S. Zhang, C. Liu, Z. Feng, G. Hu, F. Chen, T. Wan, X. Guan, T. Wu, R. Joshi, M. Li, C. Cazorla, Y. Lu, Z. Han, H. Xu, D. Chu, Lab free protein-based moisture electric generators with a high electric output, Energy Environ. Sci. 16 (2023) 2338–2345.
[68] D. Shen, M. Xiao, G. Zou, L. Liu, W.W. Duley, Y.N. Zhou, Self-powered wearable electronics based on moisture enabled electricity generation, Adv. Mater. 30 (2018) 1705925.
[69] Y. Huang, H. Cheng, C. Yang, H. Yao, C. Li, L. Qu, All-region-applicable, continuous power supply of graphene oxide composite, Energy Environ. Sci. 12 (2019) 1848–1856.
[70] Y. Wang, J. Duan, Y. Zhao, Y. Duan, Q. Tang, Self-powered PEDOT and derivate monoelectrodes to harvest rain energy, Nano Energy 41 (2017) 293–300.
[71] X. Xu, Y. Wang, P. Li, W. Xu, L. Wei, Z. Wang, Z. Yang, A leaf-mimic rain energy harvester by liquid-solid contact electrification and piezoelectricity, Nano Energy 90 (2021) 106573.
[72] Z.H. Lin, G. Cheng, S. Lee, K.C. Pradel, Z.L. Wang, Harvesting water drop energy by a sequential contact-electrification and electrostatic-induction process, Adv. Mater. 26 (2014) 4690–4696.
[73] C. Chen, Y. Kuang, L. Hu, Challenges and opportunities for solar evaporation, Joule 3 (2019) 683–718.
[74] H. Wang, Y. Sun, T. He, Y. Huang, H. Cheng, C. Li, D. Xie, P. Yang, Y. Zhang, L. Qu, Bilayer of polyelectrolyte films for spontaneous power generation in air up to an integrated 1,000 V output, Nat. Nanotechnol. 16 (2021) 811–819.
[75] F. Zhao, Y. Liang, H. Cheng, L. Jiang, L. Qu, Highly efficient moisture-enabled electricity generation from graphene oxide frameworks, Energy Environ. Sci. 9 (2016) 912–916.
[76] H. Qu, L. Wan, Z. Tian, G. Liu, Z.L. Wang, Evaporation triboelectric-nanogenerator: harvesting low-grade heat energy from ambient environment, Adv. Mater. Technol. 9 (2023) 2301409.
[77] X. Huang, K. Hayashi, M. Fujii, F. Villa, Y. Yamazaki, H. Okazawa, Identification of potential locations for small hydropower plant based on resources time footprint: a case study in Dan River Basin, China, Renew. Energy 205 (2023) 293–304.
[78] W. Wang, H. Wang, G. Liu, L. Gao, Analysis of the trade-off between hydroelectricity generation and ecological protection from the perspective of eco-efficiency in Southwest China, J. Environ. Manag. 315 (2022) 115063.
[79] E.J. Arbuckle, M. Binsted, E.G.R. Davies, D.V. Chiappori, C. Bergero, M. S. Siddiqui, C. Roney, H.C. McJeon, Y. Zhou, N. Macaluso, Insights for Canadian electricity generation planning from an integrated assessment model: should we be more cautious about hydropower cost overruns? Energy Policy 150 (2021) 112138.
[80] Z. Tang, S. Lin, Z.L. Wang, Effect of surface pre-charging and electric field on the contact electrification between liquid and solid, J. Phys. Chem. C 126 (2022) 8897–8905.
[81] Z. Tang, D. Yang, H. Guo, S. Lin, Z.L. Wang, Spontaneous wetting induced by contact-electrification at liquid-solid interface, Adv. Mater. 36 (2024) 2400451.
[82] M. Sun, Q. Lu, Z.L. Wang, B. Huang, Understanding contact electrification at liquid-solid interfaces from surface electronic structure, Nat. Commun. 12 (2021) 1752.
[83] J. Chi, C. Liu, L. Che, D. Li, K. Fan, Q. Li, W. Yang, L. Dong, G. Wang, Z.L. Wang, Harvesting water-evaporation-induced electricity based on liquid-solid triboelectric nanogenerator, Adv. Sci. 9 (2022) 2201586.
[84] J. Yin, Z. Zhang, X. Li, J. Yu, J. Zhou, Y. Chen, W. Guo, Waving potential in graphene, Nat. Commun. 5 (2014) 3582.
[85] H. Helmholtz, Ueber einige gesetze der vertheilung elektrischer ströme in körperlichen leitern mit anwendung auf die thierisch-elektrischen versuche, Ann. Phys. 165 (1853) 211–233.
[86] M. Gouy, Sur la constitution de la charge électrique à la surface d'un électrolyte, J. Phys. Theor. Appl. 9 (1910) 457–468.
[87] D.L. Chapman, A contribution to the theory of electrocapillarity, Philos. Mag. 25 (1913) 475–481.
[88] O. Stern, The theory of the electric double layer, Electrochemistry 30 (1924) 508.
[89] D.C. Grahame, The electrical double layer and the theory of electrocapillarity, Chem. Rev. 41 (1947) 441–501.
[90] S. Lin, X. Chen, Z.L. Wang, Contact Electrification at the Liquid-Solid Interface, Chem. Rev. 122 (2022) 5209–5232.
[91] L. Tong, Z. Yu, Y.J. Gao, X.C. Li, J.F. Zheng, Y. Shao, Y.H. Wang, X.S. Zhou, Local cation-tuned reversible single-molecule switch in electric double layer, Nat. Commun. 14 (2023) 3397.
[92] X. Li, Z.L. Wang, D. Wei, Scavenging energy and information through dynamically regulating the electrical double layer, Adv. Funct. Mater. (2024) 2405520.
[93] S. Li, Z. Zhang, P. Peng, X. Li, Z.L. Wang, D. Wei, A green approach to induce and steer chemical reactions using inert solid dielectrics, Nano Energy 122 (2024) 109286.
[94] S. Li, J. Liu, Z.L. Wang, D. Wei, Mechano-driven chemical reactions, Green Energy Environ. (2024).
[95] X. Li, S.X. Li, X. Guo, J.J. Shao, Z.L. Wang, D. Wei, Triboiontronics for efficient energy and information flow, Matter 6 (2023) 3912–3926.
[96] X. Li, R. Li, S. Li, Z.L. Wang, D. Wei, Triboiontronics with temporal control of electrical double layer formation, Nat. Commun. 15 (2024) 6182.
[97] H. Qin, L. Xu, S. Lin, F. Zhan, K. Dong, K. Han, H. Wang, Y. Feng, Z.L. Wang, Underwater energy harvesting and sensing by sweeping out the charges in an electric double layer using an oil droplet, Adv. Funct. Mater. 32 (2022) 2111662.
[98] Z.L. Wang, A.C. Wang, On the origin of contact-electrification, Mater. Today 30 (2019) 34–51.
[99] S. Lin, L. Xu, A. Chi Wang, Z.L. Wang, Quantifying electron-transfer in liquid-solid contact electrification and the formation of electric double-layer, Nat. Commun. 11 (2020) 399.
[100] J. Nie, Z. Ren, L. Xu, S. Lin, F. Zhan, X. Chen, Z.L. Wang, Probing contact-electrification-induced electron and ion transfers at a liquid-solid interface, Adv. Mater. 32 (2020) 1905696.
[101] J. You, J. Shao, Y. He, F.F. Yun, K.W. See, Z.L. Wang, X. Wang, High-electrification performance and mechanism of a water-solid mode triboelectric nanogenerator, ACS Nano 15 (2021) 8706–8714.
[102] S. Kumar, A. Sharma, V. Gupta, M. Tomar, Development of novel MoS_2 hydrovoltaic nanogenerators for electricity generation from moving NaCl droplet, J. Alloys Compd. 884 (2021) 161058.
[103] K. Xia, Y. Tian, J. Fu, Z. Zhu, J. lu, Z. Zhao, H. Tang, Z. Ye, Z. Xu, Transparent and stretchable high-output triboelectric nanogenerator for high-efficiency self-charging energy storage systems, Nano Energy 87 (2021) 106210.
[104] Y. Dong, M. Feng, J. Cheng, S. Chang, D. Wang, W. Lu, Ring-shaped single-electrode triboelectric nanogenerator (RSE-TENG) for energy harvesting and liquid flow rate monitoring of gas-liquid two-phase flow, Nano Energy 119 (2024) 109083.
[105] J.M. Perkel, The Internet of Things comes to the lab, Nature 542 (2017) 125–126.
[106] J. Franco, A. Aris, B. Canberk, A.S. Uluagac, A survey of honeypots and honeynets for internet of things, industrial internet of things, and cyber-physical systems, IEEE Commun. Surv. Tut. 23 (2021) 2351–2383.
[107] N. Saeed, M.S. Alouini, T.Y. Al-Naffouri, Toward the internet of underground things: a systematic survey, IEEE Commun. Surv. Tutor. 21 (2019) 3443–3466.
[108] R. Zhang, S. Wang, M.H. Yeh, C. Pan, L. Lin, R. Yu, Y. Zhang, L. Zheng, Z. Jiao, Z. L. Wang, A streaming potential/current-based microfluidic direct current generator for self-powered nanosystems, Adv. Mater. 27 (2015) 6482–6487.
[109] J.K. Moon, J. Jeong, D. Lee, H.K. Pak, Electrical power generation by mechanically modulating electrical double layers, Nat. Commun. 4 (2013) 1487.
[110] P. Jiang, L. Zhang, H. Guo, C. Chen, C. Wu, S. Zhang, Z.L. Wang, Signal output of triboelectric nanogenerator at oil-water-solid multiphase interfaces and its application for dual-signal chemical sensing, Adv. Mater. 31 (2019) 1902793.
[111] Y. Long, Y. Yu, X. Yin, J. Li, C. Carlos, X. Du, Y. Jiang, X. Wang, Effective anti-biofouling enabled by surface electric disturbance from water wave-driven nanogenerator, Nano Energy 57 (2019) 558–565.
[112] X. Zhang, Y. Zheng, D. Wang, Z.U. Rahman, F. Zhou, Liquid–solid contact triboelectrification and its use in self-powered nanosensor for detecting organics in water, Nano Energy 30 (2016) 321–329.
[113] D. Bao, Z. Wen, J. Shi, L. Xie, H. Jiang, J. Jiang, Y. Yang, W. Liao, X. Sun, An anti-freezing hydrogel based stretchable triboelectric nanogenerator for biomechanical energy harvesting at sub-zero temperature, J. Mater. Chem. A 8 (2020) 13787–13794.
[114] A. Khan, S. Ginnaram, C.H. Wu, H.W. Lu, Y.F. Pu, J.I. Wu, D. Gupta, Y.C. Lai, H. C. Lin, Fully self-healable, highly stretchable, and anti-freezing supramolecular gels for energy-harvesting triboelectric nanogenerator and self-powered wearable electronics, Nano Energy 90 (2021) 106525.
[115] Y. Wu, Y. Luo, J. Qu, W.A. Daoud, T. Qi, Liquid single-electrode triboelectric nanogenerator based on graphene oxide dispersion for wearable electronics, Nano Energy 64 (2019) 103948.
[116] W. Deng, G. Feng, L. Li, X. Wang, H. Lu, X. Li, J. Li, W. Guo, J. Yin, Capillary front broadening for water-evaporation-induced electricity of one kilovolt, Energy Environ. Sci. 16 (2023) 4442–4452.
[117] S. Fang, J. Li, Y. Xu, C. Shen, W. Guo, Evaporating potential, Joule 6 (2022) 690–701.
[118] J. Tan, X. Wang, W. Chu, S. Fang, C. Zheng, M. Xue, X. Wang, T. Hu, W. Guo, Harvesting energy from atmospheric water: grand challenges in continuous electricity generation, Adv. Mater. 36 (2024) 2211165.
[119] C. Shao, J. Gao, T. Xu, B. Ji, Y. Xiao, C. Gao, Y. Zhao, L. Qu, Wearable fiberform hygroelectric generator, Nano Energy 53 (2018) 698–705.
[120] N. Chen, Q. Liu, C. Liu, G. Zhang, J. Jing, C. Shao, Y. Han, L. Qu, MEG actualized by high-valent metal carrier transport, Nano Energy 65 (2019) 104047.
[121] H. Cheng, Y. Huang, F. Zhao, C. Yang, P. Zhang, L. Jiang, G. Shi, L. Qu, Spontaneous power source in ambient air of a well-directionally reduced graphene oxide bulk, Energy Environ. Sci. 11 (2018) 2839–2845.
[122] Y. Huang, H. Cheng, C. Yang, P. Zhang, Q. Liao, H. Yao, G. Shi, L. Qu, Interface-mediated hygroelectric generator with an output voltage approaching 1.5 volts, Nat. Commun. 9 (2018) 4166.
[123] T.G. Yun, J. Bae, H.G. Nam, D. Kim, K.R. Yoon, S.M. Han, I.D. Kim, Ion-permselective conducting polymer-based electrokinetic generators with maximized utility of green water, Nano Energy 94 (2022) 106946.
[124] T. Ding, K. Liu, J. Li, G. Xue, Q. Chen, L. Huang, B. Hu, J. Zhou, All-printed porous carbon film for electricity generation from evaporation-driven water flow, Adv. Funct. Mater. 27 (2017) 1700551.
[125] J. Li, K. Liu, T. Ding, P. Yang, J. Duan, J. Zhou, Surface functional modification boosts the output of an evaporation-driven water flow nanogenerator, Nano Energy 58 (2019) 797–802.
[126] X. Zhu, J. Hao, B. Bao, Y. Zhou, H. Zhang, J. Pang, Z. Jiang, L. Jiang, Unique ion rectification in hypersaline environment: a high-performance and sustainable power generator system, Sci. Adv. 4 (2018) eaau1665.

[127] Q. Ren, K. Chen, H. Zhu, J.F. Zhang, Z.G. Qu, Nanoparticle enhanced salinity-gradient osmotic energy conversion under photothermal effect, Energy Convers. Manag. 251 (2022) 115032.
[128] W. Zhao, Y. Wang, M. Han, J. Xu, L. Han, K.C. Tam, Osmotic energy generation with mechanically robust and oppositely charged cellulose nanocrystal intercalating GO membranes, Nano Energy 98 (2022) 107291.
[129] F. Yang, P. Peng, Z.Y. Yan, H. Fan, X. Li, S. Li, H. Liu, T.L. Ren, Y. Zhou, Z. L. Wang, D. Wei, Vertical iontronic energy storage based on osmotic effects and electrode redox reactions, Nat. Energy 9 (2024) 263–271.
[130] P. Peng, H. Qian, J. Liu, Z. Wang, D. Wei, Bioinspired ionic control for energy and information flow, Int. J. Smart Nano Mater. 15 (2024) 198–221.
[131] H. Qian, D. Wei, Z. Wang, Bionic iontronics based on nano-confined structures, Nano Res. 16 (2023) 11718–11730.
[132] R.K. Tonnah, M. Chai, M. Abdollahzadeh, H. Xiao, M. Mohammad, E. Hosseini, M. Zakertabrizi, D. Jarrahbashi, A. Asadi, A. Razmjou, M. Asadnia, Bioinspired angstrom-scale heterogeneous MOF-on-MOF membrane for osmotic energy harvesting, ACS Nano 17 (2023) 12445–12457.
[133] H. Peng, D. Wang, S. Fu, Artificial transpiration with asymmetric photothermal textile for continuous solar-driven evaporation, spatial salt harvesting and electrokinetic power generation, Chem. Eng. J. 426 (2021) 131818.
[134] X. Nie, B. Ji, N. Chen, Y. Liang, Q. Han, L. Qu, Gradient doped polymer nanowire for moistelectric nanogenerator, Nano Energy 46 (2018) 297–304.
[135] X. Yan, W. Xu, Y. Deng, C. Zhang, H. Zheng, S. Yang, Y. Song, P. Li, X. Xu, Y. Hu, L. Zhang, Z. Yang, S. Wang, Z. Wang, Bubble energy generator, Sci. Adv. 8 (2022) eabo7698.
[136] X. Wei, Z. Zhao, C. Zhang, W. Yuan, Z. Wu, J. Wang, Z.L. Wang, All-weather droplet-based triboelectric nanogenerator for wave energy harvesting, ACS Nano 15 (2021) 13200–13208.
[137] S. Li, Z. Zhang, F. Yang, X. Li, P. Peng, Y. Du, Q. Zeng, M. Willatzen, Z.L. Wang, D. Wei, Transistor-like triboiontronics with record-high charge density for self-powered sensors and neurologic analogs, Device (2024) 100332.
[138] Y. Ouyang, X. Li, S. Li, P. Peng, F. Yang, Z.L. Wang, D. Wei, Opto-iontronic coupling in triboelectric nanogenerator, Nano Energy 116 (2023) 108796.
[139] P. Peng, P. Shen, H. Qian, J. Liu, H. Lu, Y. Jiao, F. Yang, H. Liu, T. Ren, Z. Wang, D. Wei, Photochemical iontronics with multitype ionic signal transmission at single pixel for self-driven color and tridimensional vision, Device (2024) 100574.
[140] R. Li, X. Li, Z. Zhang, M. Willatzen, Z.L. Wang, D. Wei, Triboelectric Programmed Droplet Manipulation for Plug-and-Play Assembly, Adv. Funct. Mater. (2024) 2416457.
[141] Z. Ying, Y. Long, F. Yang, Y. Dong, J. Li, Z. Zhang, X. Wang, Self-powered liquid chemical sensors based on solid-liquid contact electrification, Analyst 146 (2021) 1656–1662.
[142] Z.H. Lin, G. Cheng, L. Lin, S. Lee, Z.L. Wang, Water-solid surface contact electrification and its use for harvesting liquid-wave energy, Angew. Chem. Int. Ed. 52 (2013) 12545–12549.
[143] Y. Wei, X. Li, Z. Yang, J.J. Shao, Z.L. Wang, D. Wei, Contact electrification at the solid-liquid transition interface, Mater. Today 74 (2024) 2–11.
[144] J. Yin, X.M. Li, J. Yu, Z.H. Zhang, J.X. Zhou, W.L. Guo, Generating electricity by moving a droplet of ionic liquid along graphene, Nat. Nanotechnol. 9 (2014) 378–383.
[145] S. Yang, Y. Su, Y. Xu, Q. Wu, Y. Zhang, M.B. Raschke, M. Ren, Y. Chen, J. Wang, W. Guo, Y. Ron Shen, C. Tian, Mechanism of electric power generation from ionic droplet motion on polymer supported graphene, J. Am. Chem. Soc. 140 (2018) 13746–13752.
[146] T. He, H. Wang, B. Lu, T. Guang, C. Yang, Y. Huang, H. Cheng, L. Qu, Fully printed planar moisture-enabled electric generator arrays for scalable function integration, Joule 7 (2023) 935–951.
[147] L. Yang, F. Yang, X. Liu, K. Li, Y. Zhou, Y. Wang, T. Yu, M. Zhong, X. Xu, L. Zhang, W. Shen, D. Wei, A moisture-enabled fully printable power source inspired by electric eels, PNAS 118 (2021) e2023164118.
[148] P. Peng, F. Yang, X. Li, S. Li, Z. Wang, D. Wei, High-power iontronics enabled by nanoconfined ion dynamics, Cell Rep. Phys. Sci. 5 (2024) 101824.
[149] Z.L. Wang, Triboelectric nanogenerator (TENG)–sparking an energy and sensor revolution, Adv. Energy Mater. 10 (2020) 2000137.
[150] S. Lin, X. Chen, Z.L. Wang, Electron transfer in liquid–solid contact electrification and double-layer formation. Encyclopedia of Solid-Liquid Interfaces, Elsevier, 2024, pp. 576–599.
[151] Y. Dong, S. Xu, C. Zhang, L. Zhang, D. Wang, Y. Xie, N. Luo, Y. Feng, N. Wang, M. Feng, X. Zhang, F. Zhou, Z.L. Wang, Gas-liquid two-phase flow-based triboelectric nanogenerator with ultrahigh output power, Sci. Adv. 8 (2022) eadd0464.
[152] F. Yi, X. Wang, S. Niu, S. Li, Y. Yin, K. Dai, G. Zhang, L. Lin, Z. Wen, H. Guo, J. Wang, M.H. Yeh, Y. Zi, Q. Liao, Z. You, Y. Zhang, Z.L. Wang, A highly shape-adaptive, stretchable design based on conductive liquid for energy harvesting and self-powered biomechanical monitoring, Sci. Adv. 2 (2016) e1501624.
[153] X. Luo, L. Zhu, Y.C. Wang, J. Li, J. Nie, Z.L. Wang, A flexible multifunctional triboelectric nanogenerator based on MXene/PVA hydrogel, Adv. Funct. Mater. 31 (2021) 2104928.
[154] Y. Ouyang, X. Li, S. Li, Z.L. Wang, D. Wei, Ionic rectification by dynamic regulation of the electric double layer at the hydrogel interface, ACS Appl. Mater. Interfaces 16 (2024) 18236–18244.
[155] L. Zhang, D. Wang, Triboiontronics based on dynamic electric double layer regulation, Matter 6 (2023) 3698–3699.
[156] A.S. Aji, R. Nishi, H. Ago, Y. Ohno, High output voltage generation of over 5 V from liquid motion on single-layer MoS2, Nano Energy 68 (2020) 104370.
[157] F. Zhao, H. Cheng, Z. Zhang, L. Jiang, L. Qu, Direct power generation from a graphene oxide film under moisture, Adv. Mater. 27 (2015) 4351–4357.
[158] D. Wei, Writable electrochemical energy source based on graphene oxide, Sci. Rep. 5 (2015) 15173.
[159] J. Feng, M. Graf, K. Liu, D. Ovchinnikov, D. Dumcenco, M. Heiranian, V. Nandigana, N.R. Aluru, A. Kis, A. Radenovic, Single-layer MoS2 nanopores as nanopower generators, Nature 536 (2016) 197–200.
[160] J. Hao, B. Bao, J. Zhou, Y. Cui, X. Chen, J. Zhou, Y. Zhou, L.A. Jiang, Euryhaline-fish-inspired salinity self-adaptive nanofluidic diode leads to high-performance blue energy harvesters, Adv. Mater. 34 (2022) e2203109.
[161] D. Wei, F. Yang, Z. Jiang, Z. Wang, Flexible iontronics based on 2D nanofluidic material, Nat. Commun. 13 (2022) 4965.
[162] P. Peng, F. Yang, Z. Wang, D. Wei, Integratable paper-based iontronic power source for all-in-one disposable electronics, Adv. Energy Mater. 13 (2023) 2302360.
[163] H. Qian, P. Peng, H. Fan, Z. Yang, L. Yang, Y. Zhou, D. Tan, F. Yang, M. Willatzen, G. Amaratunga, Z. Wang, D. Wei, Horizontal transport in Ti3C2Tx MXene for highly efficient osmotic energy conversion from saline-alkali environments, Angew. Chem. Int. Ed. (2024) e202414984.
[164] X. Liang, S. Liu, S. Lin, H. Yang, T. Jiang, Z.L. Wang, Liquid–solid triboelectric nanogenerator arrays based on dynamic electric-double-layer for harvesting water wave energy, Adv. Energy Mater. 13 (2023) 2300571.
[165] W. Sun, Y. Zheng, T. Li, M. Feng, S. Cui, Y. Liu, S. Chen, D. Wang, Liquid-solid triboelectric nanogenerators array and its applications for wave energy harvesting and self-powered cathodic protection, Energy 217 (2021) 119388.
[166] L. Yang, L.N.Y. Cao, S. Li, P. Peng, H. Qian, G. Amaratunga, F. Yang, Z.L. Wang, D. Wei, MOFs/MXene nano-hierarchical porous structures for efficient ion dynamics, Nano Energy 129 (2024) 110076.
[167] W. Xu, H. Zheng, Y. Liu, X. Zhou, C. Zhang, Y. Song, X. Deng, M. Leung, Z. Yang, R.X. Xu, Z.L. Wang, X.C. Zeng, Z. Wang, A droplet-based electricity generator with high instantaneous power density, Nature 578 (2020) 392–396.
[168] X. Hao, H. Yao, P. Zhang, Q. Liao, K. Zhu, J. Chang, H. Cheng, J. Yuan, L. Qu, Multifunctional solar water harvester with high transport selectivity and fouling rejection capacity, Nat. Water 1 (2023) 982–991.
[169] C. Ye, D. Liu, P. Chen, L.N.Y. Cao, X. Li, T. Jiang, Z.L. Wang, An integrated solar panel with a triboelectric nanogenerator array for synergistic harvesting of raindrop and solar energy, Adv. Mater. 35 (2023) 2209713.